CANCER

Tumor-specific GPX4 degradation enhances ferroptosis-initiated antitumor immune response in mouse models of pancreatic cancer

Jingbo Li[1,2]†, Jiao Liu[3]†, Zhuan Zhou[2], Runliu Wu[2], Xin Chen[2], Chunhua Yu[2], Brent Stockwell[4], Guido Kroemer[5,6,7], Rui Kang[2]*, Daolin Tang[2]*

Lipid peroxidation–dependent ferroptosis has become an emerging strategy for tumor therapy. However, current strategies not only selectively induce ferroptosis in malignant cells but also trigger ferroptosis in immune cells simultaneously, which can compromise anti-tumor immunity. Here, we used In-Cell Western assays combined with an unbiased drug screening to identify the compound N6F11 as a ferroptosis inducer that triggered the degradation of glutathione peroxidase 4 (GPX4), a key ferroptosis repressor, specifically in cancer cells. N6F11 did not cause the degradation of GPX4 in immune cells, including dendritic, T, natural killer, and neutrophil cells. Mechanistically, N6F11 bound to the RING domain of E3 ubiquitin ligase tripartite motif containing 25 (TRIM25) in cancer cells to trigger TRIM25-mediated K48-linked ubiquitination of GPX4, resulting in its proteasomal degradation. Functionally, N6F11 treatment caused ferroptotic cancer cell death that initiated HMGB1-dependent antitumor immunity mediated by CD8$^+$ T cells. N6F11 also sensitized immune checkpoint blockade that targeted CD274/PD-L1 in advanced cancer models, including genetically engineered mouse models of pancreatic cancer driven by *KRAS* and *TP53* mutations. These findings may establish a safe and efficient strategy to boost ferroptosis-driven antitumor immunity.

INTRODUCTION

Immunotherapy has recently changed the landscape of cancer treatment, leading to prolonged survival in certain patients (*1*). Specifically, immune checkpoint inhibitors (ICIs), such as monoclonal antibodies targeting programmed death 1 (PDCD1) or anti-CD274, also known as programmed death ligand 1 (PD-L1), have been approved as monotherapies or as part of combination treatments to stimulate antitumor CD8$^+$ T cell responses (*2*). Despite substantial advances, most patients do not respond to ICIs because of the development of an immunosuppressive tumor microenvironment, antigenic tumor heterogeneity, insufficient immunogenicity, or systemic immune failure (*3*, *4*). Therefore, there is still an unmet need for approaches that improve the response to immunotherapy.

An effective antitumor adaptive immune response requires dendritic cells (DCs) that present tumor-associated antigens to T lymphocytes. The initiation of the anticancer response by DCs largely depends on sufficient immune signals, particularly pathogen-associated molecular patterns and damage-associated molecular patterns (DAMPs) (*5*). The induction of immunogenic cell death (ICD) by chemotherapy, radiotherapy, or targeted therapies can initiate an adaptive immune response by exposing and releasing a variety of DAMPs, including representative high-mobility group box 1 (HMGB1) protein (*6*). So-called induction therapies cause ICD sensitization to subsequent treatment with ICIs (*7*). However, it is not known which type of cell death optimally enhances the immunogenicity of tumor cells.

Ferroptotic cell death depends on unrestricted lipid peroxidation rather than on the activation of apoptotic effector caspases (*8*). Glutathione peroxidase 4 (GPX4) is a master repressor of ferroptosis that reduces hydroperoxides to alcohols using reduced glutathione (GSH) as a substrate (*9*). The activation of an amino acid antiporter, solute carrier family 7 member 11 (SLC7A11/system xc$^-$), favors intracellular GSH production to sustain GPX4 activity (*10*). The most widely used ferroptosis inducers in cancer preclinical research are inhibitors of GPX4, such as RSL3, or SLC7A11, such as erastin (*11*–*14*). These inhibitors also trigger ferroptotic death in DCs, T cells, and neutrophils, dampening the antitumor immune response (*15*–*18*). Thus, the development of cancer cell–specific ferroptosis inducers is critical for overcoming side effects and increasing the treatment efficacy of ICIs (*19*).

In the study described here, we identified a small-molecule compound named N6F11 that selectively triggers ferroptosis in cancer cells, but not in DCs, T lymphocytes, and neutrophils, by activating tripartite motif containing 25 (TRIM25)–mediated degradation of GPX4 protein. We not only elucidated the mechanistic basis of TRIM25-mediated GPX4 degradation but also evaluated the effectiveness and safety of N6F11 in inducing ICD and enhancing ICI effectiveness for tumor immunotherapy.

[1]Department of Gastroenterology, Third Xiangya Hospital, Central South University, Changsha, Hunan 410013, China. [2]Department of Surgery, UT Southwestern Medical Center, Dallas, TX 75390, USA. [3]DAMP Laboratory, Third Affiliated Hospital, Guangdong Provincial Key Laboratory of Protein Modification and Degradation, Guangzhou Medical University, Guangzhou, Guangdong 510510, China. [4]Department of Chemistry, Columbia University, New York, NY 10027, USA. [5]Centre de Recherche des Cordeliers, Equipe labellisée par la Ligue contre le cancer, Université de Paris Cité, Sorbonne Université, INSERM U1138, Institut Universitaire de France, Paris, France. [6]Metabolomics and Cell Biology Platforms, Gustave Roussy Cancer Campus, 94800 Villejuif, France. [7]Pôle de Biologie, Hôpital Européen Georges Pompidou, AP-HP, F-75015 Paris, France.
*Corresponding author. Email: daolin.tang@utsouthwestern.edu (D.T.); rui.kang@utsouthwestern.edu (R.K.)
†These authors contributed equally to this work.

RESULTS

Identification of GPX4 degraders

The activity of GPX4 is critical for the prevention of ferroptosis; therefore, several GPX4 inhibitors, such as RSL3, Fin56, and ML210, have been developed to induce cell death in cancer cells (*20*). In addition to inhibiting GPX4 enzymatic activity, RSL3, Fin56, and ML210 also cause GPX4 protein degradation through different mechanisms (*9*, *21*–*24*). To identify new GPX4 protein degraders, we used an In-Cell Western assay, which is an infrared dye–based quantitative immunofluorescence assay performed in a microtiter plate, combining the specificity of Western blotting with the throughput of enzyme-linked immunosorbent assay (ELISA) (*25*). We treated PANC1 cells, a human pancreatic ductal adenocarcinoma (PDAC) cell line sensitive to ferroptosis (*22*, *26*), with 4208 synthetic compounds of unknown biological activity from Selleck Chemicals in a 96-well plate for 24 hours (Fig. 1A). After measuring the ratio of the red signal (700 nm) of GPX4 and the green signal (800 nm) of actin beta (ACTB) as control, we determined that 14 compounds inhibited GPX4, but not ACTB, protein abundance to 50%, whereas eight compounds induced GPX4 protein abundance more than twofold greater than control (Fig. 1B and fig. S1A).

Next, we used traditional immunoblots and the same anti-GPX4 antibody in an In-Cell Western assay to validate the top compound candidates in PANC1 cells and determined that N6F11 most efficiently inhibited the abundance of GPX4 protein. The ability of N6F11 (0.625 to 5μM) to suppress the abundance of GPX4 protein was confirmed in multiple human or mouse tumor cell lines, including PANC1 (human PDAC cells), HT1080 (human fibrosarcoma cells), MiaPACA2 (human PDAC cells), BxPC3 (human PDAC cells), KPC (mouse PDAC cells), 5637 (human bladder carcinoma cells), Hs578T (human breast cancer cells), and HeLa (human cervical cancer cells) (Fig. 1C), indicating that N6F11 has a broad-spectrum activity. The down-regulation of GPX4 protein by N6F11 was accompanied by an upward shift of the GPX4 band in some cells, possibly due to changes in GPX4's isoforms or modifications (*27*). The down-regulation of GPX4 protein induced by N6F11 (Fig. 1D) was not accompanied by a reduction of *GPX4* mRNA (Fig. 1E) but rather by varying degrees of decrease in cell viability (Fig. 1F). Cycloheximide chase assays indicated that the protein half-life of GPX4 became shorter in PANC1 and HT1080 cells after N6F11 treatment ($P < 0.05$; Fig. 1, G and H). The specificity of anti-GPX4 antibody used in the In-Cell Western and immunoblot assay was verified in inducible *Gpx4*$^{-/-}$ Pfa-1 cells (Fig. 1I). Together, N6F11 suppresses GPX4 expression through enhanced protein degradation instead of through reduced gene transcription.

N6F11 induces ferroptosis

Although GPX4 is increasingly being found to play a role in inhibiting ferroptosis, in some cases, the lack of *Gpx4* in vivo also causes nonferroptotic cell death, such as apoptosis, pyroptosis, or necroptosis (*28*–*31*). To define the mechanism of N6F11-induced cell growth inhibition (Fig. 2A), we measured cell death by staining with the vital dye propidium iodide (PI). Treatment with N6F11 for 12 hours resulted in 40% death of PANC1 cells (Fig. 2, B and C, and fig. S1B). This cytotoxicity of N6F11 was blocked by ferroptosis inhibitors (liproxstatin-1, ferrostatin-1, and deferoxamine) but not by inhibitors of apoptosis (Z-VAD-FMK) and necroptosis (necrosulfonamide) (Fig. 2, B and C). Flow cytometry assays using annexin V/PI staining further confirmed that N6F11-induced PI-positive cells were inhibited by treatment with ferrostatin-1 (fig. S1C).

The chromatin-binding protein HMGB1 is a DAMP and immune mediator released by ferroptotic cells (*32*). N6F11 triggered the release of HMGB1, and this effect was blocked by ferroptosis inhibitors but not by inhibitors of other cell death modalities (Fig. 2D). Immunoblot analyses confirmed that N6F11 failed to activate the core biochemical events of apoptosis, including the cleavage of caspase-3 and poly(adenosine diphosphate–ribose) polymerase 1 (PARP), and necroptosis, such as phosphorylation of mixed-lineage kinase domain-like pseudokinase (MLKL) (Fig. 2, E and F). In contrast, N6F11 induced lipid peroxidation, as measured by two fluorescence probes: BODIPY-C11 (Fig. 2, G and H) and Click-iT linoleamide alkyne (LAA) (Fig. 2, I and J). Liproxstatin-1, a radical-trapping antioxidant, inhibited N6F11-induced lipid peroxidation (Fig. 2, G and H).

In ferroptosis, oxidative damage is usually accompanied by activation of the nuclear factor erythroid 2 (NFE2)–like BZIP transcription factor 2 (NFE2L2; also known as NRF2) pathway (*33*, *34*), endoplasmic reticulum stress (*22*, *35*), and autophagy (*36*–*39*). N6F11 induced the protein expression of NFE2L2, markers of endoplasmic reticulum stress, such as DNA damage–inducible transcript 3 (DDIT3; also known as CHOP), phosphorylated eukaryotic translation initiation factor 2 alpha kinase 3 (EIF2AK3; also known as PERK), phosphorylated EIF2A, and microtubule-associated protein 1 light chain 3 beta (MAP1LC3A/B-II, a marker of autophagosomes) (Fig. 2K). However, chloroquine, an antimalarial drug that inhibits autophagic flux by decreasing autophagosome-lysosome fusion, failed to interfere with N6F11-induced cell death (Fig. 2, B and C). The protein expression of other key ferroptosis regulators, such as cytochrome P450 oxidoreductase (POR) (*40*, *41*), apoptosis-inducing factor mitochondria-associated 2 (AIFM2) (*42*–*44*), and tumor protein 53 (TP53) (*13*, *45*), was also not affected by N6F11 (Fig. 2K). Consistent with previous studies (*21*, *36*, *39*), chloroquine, but not Z-VAD-FMK and necrosulfonamide, inhibited erastin-, RSL3-, or Fin56-induced cell death (Fig. 2L). Thus, these data suggest that N6F11 may induce autophagy-independent ferroptosis.

N6F11 induces proteasomal degradation of GPX4

We then sought to determine how N6F11 triggers GPX4 protein degradation for ferroptosis. There was no similarity in the chemical structure among N6F11, RSL3, Fin56, and erastin (fig. S2A), although they all caused different degrees of GPX4 protein degradation (*21*, *23*, *46*). We used a cellular thermal shift assay (CETSA) to examine the potential direct binding of N6F11 to GPX4. Unlike RSL3 (as a positive control), the thermal stability of GPX4 protein was not affected by erastin (negative control) and N6F11 (fig. S2, B, and C). Moreover, N6F11 failed to directly inhibit GPX activity (fig. S2D) and did not inhibit GSH production from cells (fig. S2E).

Because cell death leads to the degradation of proteins, we investigated the effect of ferroptosis inhibitors (liproxstatin-1 and tocopherol) on N6F11-induced GPX4 protein degradation. Both liproxstatin-1 and tocopherol inhibited the degradation of GPX4 protein induced by RSL3, but not by N6F11 (fig. S2F), indicating that N6F11-induced GPX4 protein degeneration is not secondary to ferroptosis. N6F11 did not trigger the release of GPX4 into cell

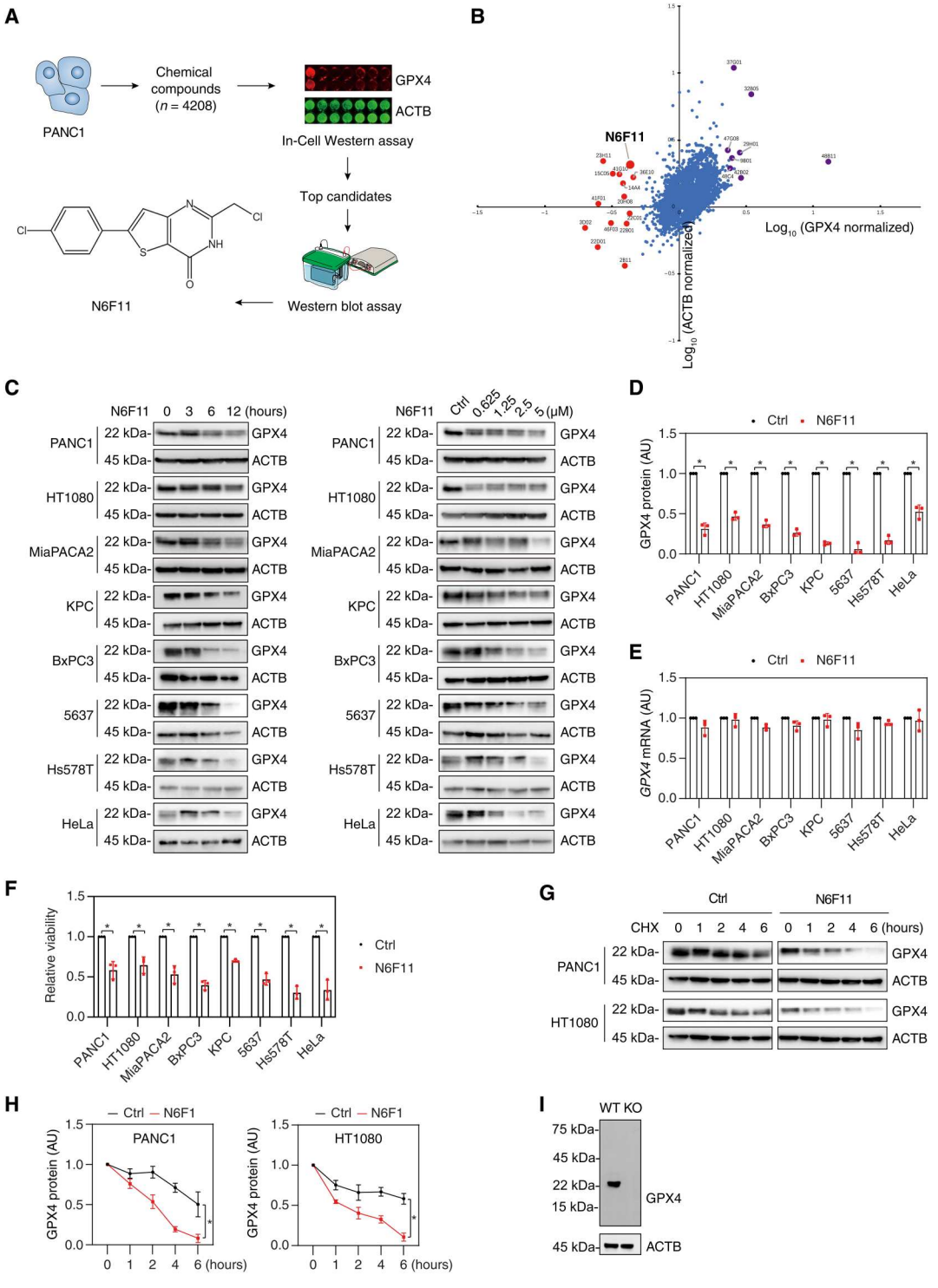

Fig. 1. Identification of N6F11 as a GPX4 degrader. (**A**) Flow chart of our screening strategy. Human PANC1 cancer cells were treated with 4208 unknown target compounds (5 μM) from Selleck Chemicals in a 96-well plate for 24 hours. In situ expression of GPX4 (red) and ACTB (green) was determined by quantitative In-Cell Western assay. The effect of the top compound candidates on GPX4 protein expression was further examined by traditional Western blot analysis. (**B**) Identification of 14 compounds that inhibit GPX4 protein expression (red) and eight compounds that increase GPX4 protein expression (purple). The structures of these compounds are shown in fig. S1. The *x* and *y* axes are $\log_{10}$ values of the normalized fluorescent signal intensity of GPX4 and ACTB, respectively. (**C**) Western blot analysis of GPX4 expression in indicated cells after treatment with 5 μM N6F11 for 3 to 12 hours or 0.625 to 5 μM N6F11 for 12 hours. (**D**) Quantitative analysis of GPX4 protein expression in indicated cells after treatment with N6F11 (5 μM) for 12 hours ($n = 3$ biologically independent samples; $^*P < 0.05$, *t* test; data are presented as mean ± SD). Ctrl, control; AU, arbitrary units. (**E**) A quantitative polymerase chain reaction analysis of *GPX4* mRNA in indicated cells after treatment with N6F11 (5 μM) for 12 hours ($n = 3$ biologically independent samples; data are presented as mean ± SD). (**F**) Cell viability analysis of indicated cells after treatment with N6F11 (5 μM) for 12 hours ($n = 3$ biologically independent samples; $^*P < 0.05$, *t* test; data are presented as mean ± SD). (**G**) Effects of N6F11 (5 μM) on GPX4 protein stability in indicated cells by the cycloheximide (CHX) chase assay. (**H**) Quantification of the data from (G) ($n = 3$ biologically independent samples; $^*P < 0.05$, one-way ANOVA test; data are presented as mean ± SD). (**I**) Identification of anti-GPX4 antibody specificity using wild-type (WT) and $Gpx4^{-/-}$ [knockout (KO)] Pfa-1 cells.

culture supernatants (fig. S2G). Fin56 is a GPX4 degrader that can be reversed by 5-tetradecyl-oxy-2-furoic acid (TOFA), an allosteric inhibitor of acetyl-CoA carboxylase alpha (*23*). However, TOFA failed to reverse N6F11-induced GPX4 degradation (fig. S2H).

Two main pathways degrade cellular proteins in eukaryotic cells: the ubiquitin-proteasome system (UPS) and autophagy. In some cases, excessive autophagy can promote ferroptosis by degrading anti-ferroptotic regulators (*47*). However, the late-stage autophagy inhibitor chloroquine failed to inhibit N6F11-induced cell death (Fig. 2L). To further determine whether autophagy is involved in N6F11-induced GPX4 protein degradation, we used mouse embryonic fibroblasts (MEFs) that lack essential autophagy genes

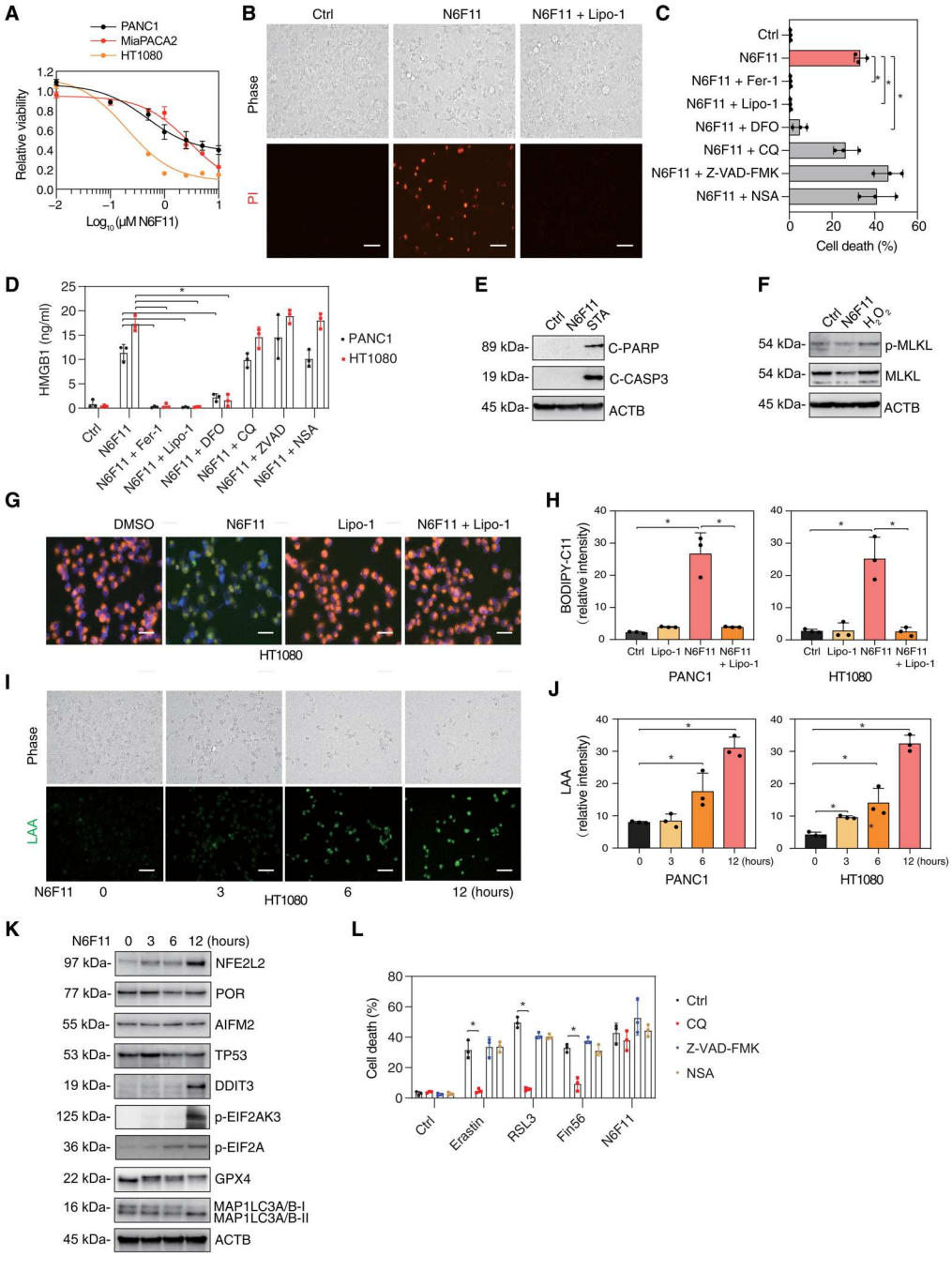

Fig. 2. N6F11 induces ferroptosis. (**A**) Cell viability of indicated cells after treatment with N6F11 for 24 hours ($n = 3$ biologically independent samples; data are presented as mean ± SD). (**B**) PI staining for cell death analysis of PANC1 cells after treatment with N6F11 (5 μM) in the absence or presence of liproxstatin-1 (Lipo-1; 1 μM), ferrostatin-1 (Fer-1; 1 μM), deferoxamine (DFO; 100 μM), Z-VAD-FMK (ZVAD; 10 μM), necrosulfonamide (NSA; 1 μM), or chloroquine (CQ; 50 μM) for 12 hours. Scale bars, 50 μm. (**C**) Quantification of the data from (B) ($n = 3$ biologically independent samples; $^*P <$ 0.05, one-way ANOVA test; data are presented as mean ± SD). (**D**) ELISA assay of HMGB1 release in indicated cells under the same conditions as described in (C) ($n = 3$ biologically independent samples; $^*P <$ 0.05, one-way ANOVA test; data are presented as mean ± SD). (**E**) Western blot analysis of indicated protein expression in PANC1 cells after treatment with N6F11 (5 μM; 12 hours) or staurosporine (STA; 0.5 μM; 12 hours). (**F**) Western blot analysis of indicated protein expression in PANC1 cells after treatment with N6F11 (5 μM; 12 hours) or H_2O_2 (1.5 mM; 2 hours). (**G**) BODIPY-C11 staining for lipid peroxidation analysis of cancer cells after treatment with N6F11 in the absence or presence of liproxstatin-1 for 6 hours. Scale bars, 50 μm. (**H**) Quantification of the data from (G) ($n = 3$ biologically independent samples; $^*P < 0.05$, one-way ANOVA test; data are presented as mean ± SD). (**I**) Click-iT LAA staining for lipid peroxidation analysis of cancer cells after treatment with N6F11 in the absence or presence of liproxstatin-1 for 6 hours. Scale bars, 50 μm. (**J**) Quantification of the data from (I) ($n = 3$ biologically independent samples; $^*P < 0.05$, one-way ANOVA test; data are presented as mean ± SD). Scale bars, 50 μm. (**K**) Western blot analysis of indicated protein expression in PANC1 cells after treatment with N6F11 (5 μM) for 3 to 12 hours. (**L**) Cell death analysis of PANC1 cells after treatment with N6F11 (5 μM), erastin (1 μM), Fin56 (5 μM), or RSL3 (0.5 μM) in the absence or presence of Z-VAD-FMK (10 μM), necrosulfonamide (NSA; 1 μM), or chloroquine (CQ; 50 μM) for 12 hours ($n = 3$ biologically independent samples; $^*P < 0.05$, one-way ANOVA test; data are presented as mean ± SD).

(genotypes: *Atg5*$^{-/-}$ or *Atg7*$^{-/-}$). The production of MAP1LC3A/B-II induced by N6F11 was limited by the loss of *Atg5* or *Atg7* and increased with the use of chloroquine, demonstrating its bioactivity (Fig. 3A and Fig. S2I). However, N6F11-induced GPX4 protein degradation and cell death were not reversed by genetic or pharmacological inhibition of autophagy (Fig. 3A and Fig. S2I), indicating that autophagy is dispensable for N6F11-promoted ferroptosis (Fig. 3B). As a positive control (*39*), *Atg5*$^{-/-}$ and *Atg7*$^{-/-}$ MEFs were resistant to erastin-, RSL3-, or Fin56-induced cell death when compared with wild-type MEFs (Fig. 3B).

Next, we analyzed the impact of the UPS on N6F11-induced GPX4 protein degradation. Treatment with bortezomib or carfilzomib, two proteasome inhibitors approved for the treatment of specific cancers (*48*), blocked N6F11-induced GPX4 protein degradation in PANC1 and HT1080 cells but failed to reverse RSL3- or Fin56-induced GPX4 protein degradation (Fig. 3C). The initial step in UPS-mediated protein degradation is the binding of

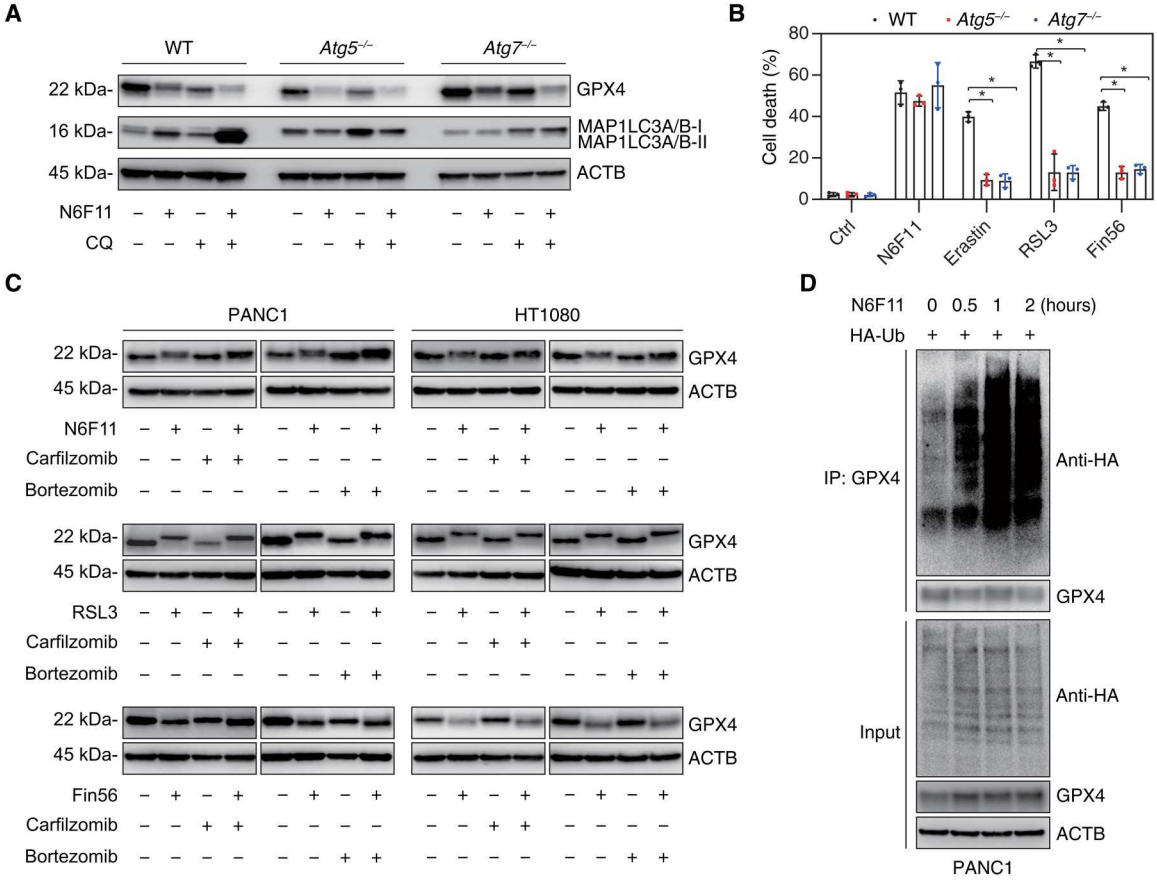

Fig. 3. Autophagy is not required for N6F11-induced GPX4 degradation and ferroptosis. (**A**) Western blot analysis of protein expression in indicated MEFs after treatment with N6F11 (5 μM) in the absence or presence of chloroquine (CQ; 50 μM) for 12 hours. (**B**) Cell death analysis of indicated MEFs after treatment with N6F11 (5 μM), erastin (1 μM), RSL3 (0.5 μM), or Fin56 (2 μM) for 24 hours ($n = 3$ biologically independent samples; $^*P < 0.05$, two-way ANOVA test; data are presented as mean ± SD). (**C**) Western blot analysis of GPX4 expression in PANC1 or HT1080 cells after treatment with N6F11 (5 μM), Fin56 (5 μM), or RSL3 (0.5 μM) in the absence or presence of carfizomib (100 nM) or bortezomib (25 nM) for 12 hours. (**D**) An IP assay was performed to verify ubiquitin (Ub) modification of GPX4 in PANC1 cells after treatment with N6F11 (5 μM) for 0.5 to 2 hours.

ubiquitin to the target protein. Immunoprecipitation experiments confirmed that the binding of GPX4 to ubiquitin was induced by N6F11 as early as 0.5 to 2 hours without the degradation of GPX4 protein (Fig. 3D). These results suggest that N6F11-induced early ubiquitination of GPX4 may lead to subsequent degradation of GPX4 protein through the proteasome rather than autophagy.

TRIM25 mediates GPX4 degradation for ferroptosis

Ubiquitination and deubiquitination are counter-balancing processes that determine protein degradation through the UPS. We first assayed the effects of N6F11 on deubiquitinases, including tumor necrosis factor–induced protein 3 (TNFAIP3/A20), ubiquitin-specific peptidase 7 (USP7), cyld lysine 63 deubiquitinase (CYLD), ubiquitin C-terminal hydrolase L1 (UCHL1), UCHL3, USP1, USP10, and USP14. In PANC1 and HT1080 cells, the total protein abundance of these deubiquitinases was not changed by N6F11, erastin, RSL3, or Fin56 (fig. S3, A and B). However, N6F11, RSL3, or Fin56 selectively induced the phosphorylation of CYLD in PANC1 and HT1080 cells (fig. S3, A and B).

Because CYLD undergoes time-dependent phosphorylation by N6F11 (fig. S3C), we examined the role of CYLD in N6F11-induced GPX4 protein degradation. Liproxstatin-1 inhibited RSL3- or Fin56-induced but failed to inhibit N6F11-induced phosphorylation of CYLD (fig. S3, D and E). Subsequent RNA interference experiments showed that the knockdown of *CYLD* (fig. S3F) had no effects on cell viability (fig. S3G) and GPX4 protein degradation in response to N6F11 (fig. S3H).

Because E3 ubiquitin ligases catalyze the transfer of ubiquitin on substrate proteins, we used immunoprecipitation in combination with mass spectrometry (IP-MS) to identify the key E3 ligases responsible for N6F11-induced proteasomal degradation of GPX4. IP-MS identified GPX4-binding proteins in PANC1 cells, including 52 E2/E3 enzymes. Among them, EIF3I and TRIM25 were also listed as GPX4-binding proteins in a publicly accessible protein-protein interaction database (http://iid.ophid.utoronto.ca/#analyze_PPIs) (Fig. 4A). Only the knockdown of *TRIM25* (Fig. 4B), but not *EIF3I* (fig. S4, A and B), abrogated the anticancer activity of N6F11 (Fig. 4C). N6F11 treatment for 1 hour increased the immunoprecipitated detectable interaction between TRIM25 and GPX4, although GPX4 protein was not degraded at this time (Fig. 4D). The N6F11-induced degradation of GPX4 protein at 3 to 12 hours was blocked in *TRIM25*-knockdown cells (Fig. 4E).

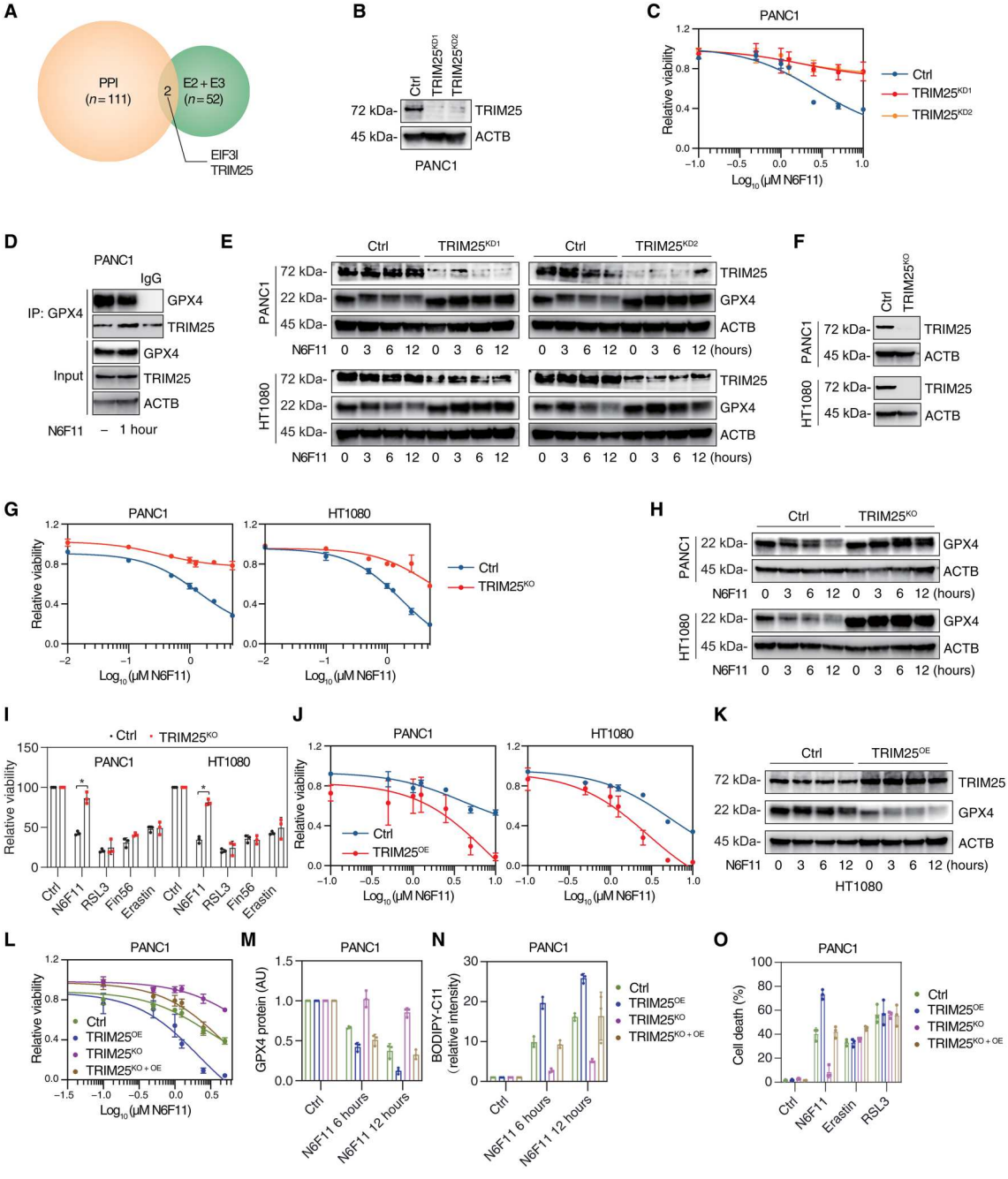

Fig. 4. TRIM25 mediates N6F11-induced GPX4 degradation and ferroptosis. (**A**) Venn diagrams of the number of GPX4-binding proteins in the public protein-protein interaction database and E2/E3 identified in PANC1 cells from mass spectrometry assay. (**B**) Western blot analysis of TRIM25 expression in indicated wild-type and *TRIM25*-knockdown (TRIM25^{KD}) cells. (**C**) Cell viability of indicated cells after treatment with N6F11 for 24 hours (n = 3 biologically independent samples; data are presented as mean ± SD). (**D**) IP analysis of the binding between TRIM25 and GPX4 in PANC1 cells in the absence or presence of N6F11 (5 μM) for 1 hour. (**E**) Western blot analysis of GPX4 expression in indicated wild-type and *TRIM25*-knockdown (TRIM25^{KD}) cells after treatment with N6F11 (5 μM) for 3 to 12 hours. (**F**) Western blot analysis of TRIM25 expression in indicated wild-type and *TRIM25*-knockout (TRIM25^{KO}) cells. (**G**) Cell viability of indicated wild-type and *TRIM25*-knockout (TRIM25^{KO}) cells after treatment with N6F11 for 24 hours (n = 3 biologically independent samples; data are presented as mean ± SD). (**H**) Western blot analysis of GPX4 expression in indicated wild-type and *TRIM25*-knockout (TRIM25^{KO}) cells after treatment with N6F11 (5 μM) for 3 to 12 hours. (**I**) Cell viability of indicated wild-type and *TRIM25*-knockout (TRIM25^{KO}) cells after treatment with N6F11 (5 μM), RSL3 (0.5 μM), Fin56 (2 μM), or erastin (5 μM) for 24 hours (n = 3 biologically independent samples; *P < 0.05, t test; data are presented as mean ± SD). (**J**) Cell viability of indicated wild-type and *TRIM25*-overexpressing (TRIM25^{OE}) cells after treatment with N6F11 for 24 hours (n = 3 biologically independent samples; data are presented as mean ± SD). (**K**) Western blot analysis of GPX4 expression in indicated wild-type and *TRIM25*-overexpressing (TRIM25^{OE}) cells after treatment with N6F11 for 3 to 12 hours. (**L**) Cell viability of indicated cells after treatment with N6F11 for 24 hours (n = 3 biologically independent samples; data are presented as mean ± SD). (**M**) GPX4 expression in indicated cells after treatment with N6F11 for 6 to 12 hours. (**N**) BODIPY-C11 amount in indicated cells after treatment with N6F11 for 6 to 12 hours. (**O**) Cell death of indicated cells after treatment with N6F11 (5 μM), RSL3 (0.5 μM), or erastin (5 μM) for 24 hours (n = 3 biologically independent samples; data are presented as mean ± SD).

CRISPR-Cas9–mediated *TRIM25* knockout (Fig. 4F) also interfered with N6F11-induced growth inhibition (Fig. 4G) and GPX4 protein degradation (Fig. 4H) in PANC1 or HT1080 cells. In sharp contrast, the knockout or knockdown of *TRIM25* failed to reverse growth inhibition by RSL3, Fin56, or erastin (Fig. 4I and Fig. S4C). Moreover, the overexpression of *TRIM25* enhanced N6F11-induced growth inhibition (Fig. 4J) and GPX4 protein degradation (Fig. 4K) in PANC1 or HT1080 cells. Together with a rescue experiment to restore the expression of *TRIM25* ($TRIM25^{KO+OE}$) and N6F11 activity in *TRIM25*-knockout cells (Fig. 4, L to O), these data indicate that TRIM25 selectively favors N6F11-induced GPX4 protein degradation and subsequent ferroptosis.

A single E3 ligase may target multiple substrates. Recent studies reported that TRIM25 is involved in the proteasomal degradation of receptor-interacting serine/threonine kinase 3 (RIPK3) during necroptosis (*49*). However, we did not observe changes in the abundance of RIPK3 protein in N6F11-treated PANC1 cells when *TRIM25* was overexpressed (fig. S4D). N6F11, RSL3, or erastin similarly killed wild-type and $Ripk3^{-/-}$ MEFs (fig. S4E). As a positive control, growth inhibition caused by CCT137690 [a necroptosis inducer (*50*)] was blocked in $Ripk3^{-/-}$ MEFs (fig. S4E). Moreover, the knock-in of *GPX4*, but not *RIPK3*, in *TRIM25*-overexpressing cells restored cell death resistance to N6F11 (fig. S4F), supporting GPX4 as a key TRIM25 substrate responsible for the regulation of ferroptosis.

GPX4 is a type of selenoenzyme that relies on the presence of selenium to effectively prevent lipid peroxidation (*51*). To determine whether TRIM25 influences selenium uptake, we measured the amount of intracellular selenium. We did not observe an increase in selenium uptake by N6F11 (fig. S4G). In contrast, N6F11 caused the down-regulation of intracellular selenium (fig. S4G). The depletion of *TRIM25* had no further effect on selenium amount compared to wild-type cells (fig. S4G). The antioxidative activity of GPX4 depends on a selenocysteine residue at 46 (U46) (*52*). Similar to wide-type control, N6F11 also induced the degradation of the GPX4 Sec/Ser (U46S) mutant protein in PANC1 cells (fig. S4H).

TRIM25 mediates K48-linked polyubiquitination of GPX4

As a member of the TRIM family of proteins, TRIM25 contains a RING-finger domain, a coiled-coil domain, and a PRY/SPRY (PS) domain (*53*). We generated truncated mutants of TRIM25 to dissect functional domains of the TRIM25-GPX4 interaction (Fig. 5A). An immunoprecipitation assay showed that only TRIM25 C-terminal mutants containing the PS domain interacted with GPX4, whereas the mutant lacking the PS domain (ΔPS) failed to bind GPX4 in cells after treatment with N6F11 for 1 hour (Fig. 5, B and C). Hence, the PS domain is required for the interaction between TRIM25 and GPX4 before GPX4 degradation.

To further investigate whether TRIM25 acts as an E3 ligase to regulate GPX4 degradation because of N6F11, we generated an E3 ligase–defective TRIM25 mutant by mutating cysteines 50 and 53 to serine (denoted as $TRIM25^{CS5}$) (*49*, *54*). $TRIM25^{CS5}$ promoted neither N6F11-induced cell growth inhibition (Fig. 5D) nor the downregulation of GPX4 protein (Fig. 5E) in cells.

TRIM25 can catalyze the formation of K48- or K63-linked ubiquitin chains (*55*, *56*). To clarify the type of polyubiquitination, green fluorescent protein (GFP)–GPX4, together with HA-ubiquitin (HA-Ub) (wild-type, K48 only, and K63 only), were transfected into 293T cells in the presence or absence of exogenous *TRIM25*. TRIM25 mainly induced immunoprecipitation-detectable K48-linked, and not K63-linked, polyubiquitination of GPX4 (Fig. 5F). To further define the potential ubiquitination site on GPX4, five mutants (K48, K125, K127, K135, and K151) were constructed on the basis of predictors of potential ubiquitination sites (http://bdmpub.biocuckoo.org/results.php). Only the K48R GPX4 mutant lost the ability to be ubiquitinated by TRIM25 (Fig. 5G), suggesting that N6F11 induces TRIM25-mediated GPX4 ubiquitination on K48. Functionally, K48R GPX4 was resistant to N6F11-induced (but not erastin- or RSL3-induced) cell death and lipid peroxidation (Fig. 5, H and I).

The TRIM25 protein can be activated with ubiquitin-conjugating enzyme (E2) Ubc5 (*57*). To elucidate the E2 type of GPX4 ubiquitination by TRIM25, an in vitro ubiquitination assay was performed with purified FLAG-TRIM25 protein with E2 UbcH5b (also known as UBE2D2) and His-GPX4 (Fig. 5J). N6F11 induced TRIM25-UbcH5b–mediated GPX4 ubiquitination (Fig. 5K). Even when it was incubated for 5 min, N6F11 also enhanced UbcH5b-dependent GPX4 ubiquitination (Fig. 5L). These results suggest that N6F11 activates the UbcH5b-TRIM25-GPX4 ubiquitination cascade.

Binding of N6F11 to TRIM25 selectively induces cancer cell death

In the next round of experiments, we determined whether N6F11 directly binds to TRIM25 to enhance its E3 ligase activity. Online molecular docking software (https://playmolecule.com/BindScope/) predicted a direct interaction between N6F11 and TRIM25. According to this molecular modeling, the RING domain of TRIM25 exhibited the highest value of ΔG and ligand efficiency compared with the other two domains, suggesting that N6F11 binds to the RING domain (Fig. 6A). CETSA confirmed that N6F11 (but not RSL3 and Fin56) increased the thermal stability of the TRIM25 protein (Fig. 6B). The depletion of the RING domain of TRIM25 reduced N6F11-mediated thermal stabilization of the TRIM25 protein (Fig. 6C). Thus, N6F11 might act as an activator of TRIM25 by binding to its RING domain.

The Human Protein Atlas (https://proteinatlas.org/) showed that the mRNA expression of *TRIM25* exceeded 50 transcripts per million in most human cancer cell lines (Fig. 6D). However, except for neutrophils, *TRIM25* mRNA expression in immune cells was typically below five transcripts per million (Fig. 6E). Immunoblots confirmed that, compared with cancer cells (HT1080, PANC1, MiaPACA2, and Calu-1), TRIM25 protein was relatively low abundance in primary human peripheral blood $CD8^+$ T cells, natural killer (NK) cells, DCs, and neutrophils (Fig. 6F). N6F11-induced cell death was restricted in DC, T, NK cells, or neutrophils compared with erastin, RSL3, and Fin56 treatment (Fig. 6G). Moreover, the overexpression of *TRIM25* by electroporation restored N6F11 toxicity in human $CD8^+$ T cells (Fig. 6, H and I).

We further determined the chemical structure of the pro-ferroptotic activity of N6F11. By modifying the chlorine group between the two nitrogens with different substituents, several analogs were synthesized (fig. S5A). These analogs did not show the same effect as N6F11 with respect to GPX4 degradation (fig. S5B) and cell growth inhibition (fig. S5C), indicating that this chloride group may be critical for N6F11 activity.

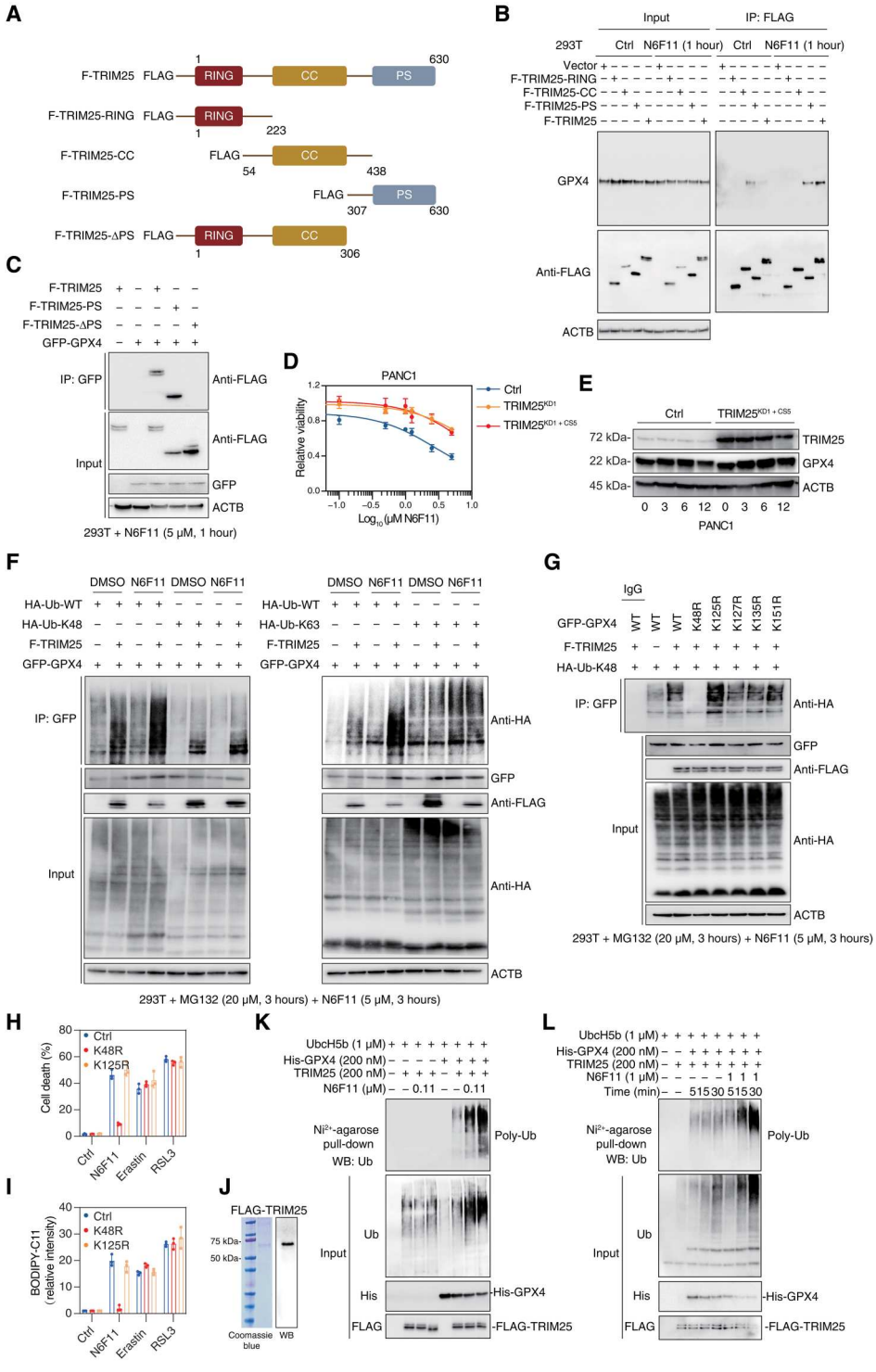

Fig. 5. Structure basis for TRIM25-mediated GPX4 degradation. (**A**) Schematic of Flag-TRIM25 and different truncations. (**B**) Different truncations or vectors of Flag-TRIM25 were transfected into 293T cells. IP assay of the binding of Flag to GPX4 in 293T cells after treatment with N6F11 for 1 hour. (**C**) Flag-TRIM25, F-TRIM25-PS, F-TRIM25-ΔPS, and GFP-GPX4 were transfected into 293T cells. IP assay of the binding of GFP to FLAG in 293T cells after treatment with N6F11 for 1 hour. (**D**) Cell viability of indicated cells after treatment with N6F11 for 24 hours (n = 3 biologically independent samples; data are presented as mean ± SD). (**E**) Western blot (WB) analysis of GPX4 expression in indicated cells after treatment with N6F11 (5 μM) for 3 to 12 hours. (**F**) 293T cells were transfected with GFP-GPX4 and HA-Ub [wild-type (WT), K48 only, or K63 only] with or without Flag-TRIM25. IP assay of the binding of GFP to HA after treatment with N6F11 and MG132 for 3 hours. (**G**) 293T cells were transfected with GFP-GPX4 (WT or its mutants) with or without Flag-TRIM25 and HA-Ub-K48. IP analysis of the binding of GFP to HA after treatment with N6F11 and MG132 for 3 hours. (**H**) Cell death analysis of indicated GPX4 WT and mutant PANC1 cells after treatment with N6F11 (5 μM), RSL3 (0.5 μM), or erastin (5 μM) for 24 hours (n = 3 biologically independent samples; data are presented as mean ± SD). (**I**) BODIPY-C11 analysis of indicated GPX4 WT and mutant PANC1 cells after treatment with N6F11 (5 μM), RSL3 (0.5 μM), or erastin (5 μM) for 6 hours (n = 3 biologically independent samples; data are presented as mean ± SD). (**J**) Purification of FLAG-TRIM25 protein of 293T cells. The left shows staining of the SDS–polyacrylamide gel electrophoresis gel of purified TRIM25 protein (~65 kD) with Coomassie blue. The right shows a Western blot band using anti-FLAG antibody. (**K**) Ubiquitination activities of TRIM25, UbcH5b, and His-GPX4 in the absence or presence of N6F11. The UbcH5b was precharged with ubiquitin. The reaction contained 5 mM Mg–adenosine triphosphate (ATP) and incubated for 25 min at 37°C. (**L**) Ubiquitination activities of TRIM25, UbcH5b, and His-GPX4 in the absence or presence of N6F11. The UbcH5b was precharged with ubiquitin. The reaction contained 5 mM Mg-ATP and was incubated for 5, 15, and 30 min at 37°C.

N6F11 treatment elicits tumor-specific T cell responses

Although N6F11 suppressed the growth of human PDAC (PANC1 or MiaPACA2) cells measured by colony formation assays (fig. S6, A and B) or the formation of three-dimensional (3D) spheroids (fig. S6, C and D), the potential role of this compound on the interaction between tumors and the adaptive immune system is unknown. To explore whether N6F11 has immunogenic properties, we tested its effects on tumors formed from an N6F11-sensitive mouse KPC cell line. We inoculated KPC cells subcutaneously into immunocompetent C57BL/6J mice. Three days after tumor inoculation (when the tumor volume was ~50 mm^3), the administration of N6F11 inhibited tumor growth compared with the control vehicle ($P < 0.0001$; Fig. 7A) and was accompanied by increased serum HMGB1 ($P = 0.0003$; Fig. 7B), increased tumor malondialdehyde [MDA; a

A

Domain	pKd (std.)	ΔG [kcal/mol] (std.)	Lig. efficiency [kcal/mol]
RING	9.02 (2.14)	−12.18 (−2.88)	−0.64
CC	7.29 (0.36)	−9.85 (−0.48)	−0.52
PS	5.98 (1.59)	−8.07 (−2.15)	−0.42

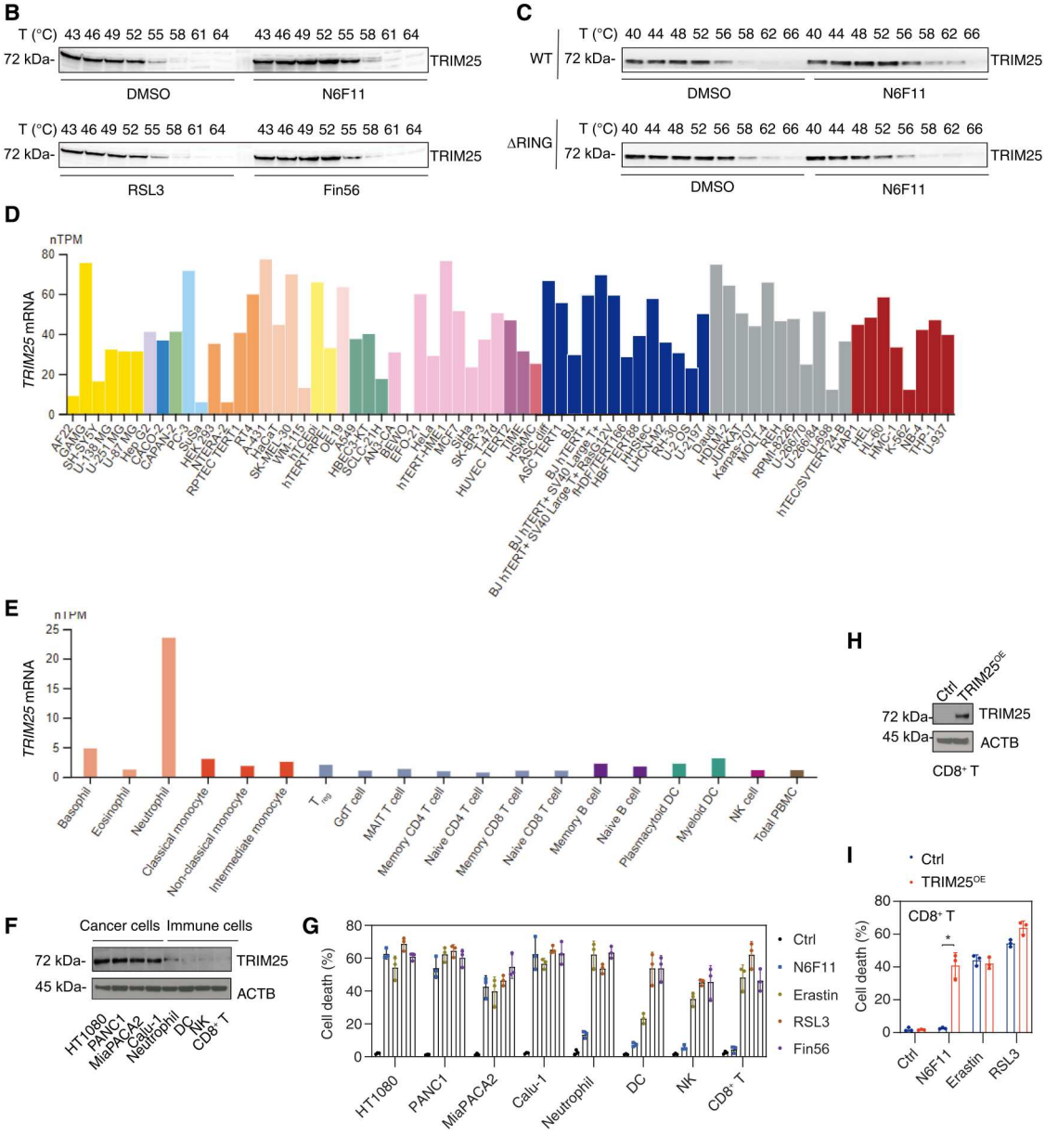

Fig. 6. Binding of N6F11 to TRIM25 selectively induces cancer cell death. (**A**) Predicted binding parameters of each domain are presented in the table. (**B**) Effects of indicated compounds on thermal stability of the TRIM25 protein in PANC1 cells. (**C**) Effects of N6F11 (10 μM) on thermal stability of the TRIM25 protein or the depletion of the RING domain of TRIM25 in PANC1 cells. (**D**) *TRIM25* mRNA expression in human cancer cell lines based on analysis of the Human Protein Atlas database. (**E**) *TRIM25* mRNA expression in normal immune cells based on analysis of the Human Protein Atlas database. T_{reg}, regulatory T cell; PBMC, peripheral blood mononuclear cell; MAIT, mucosal-associated invariant T cells. (**F**) Western blot analysis of TRIM25 protein expression in indicated human cancer cell lines and normal immune cells. (**G**) Cell death analysis of indicated cells after treatment with N6F11 (5 μM), erastin (5 μM), RSL3 (0.5 μM), or Fin56 (5 μM) for 24 hours ($n = 3$ biologically independent samples; data are presented as mean ± SD). (**H**) Western blot analysis of TRIM25 expression in control and TRIM25-overexpressing $CD8^+$ T cells. (**I**) Cell death analysis of indicated $CD8^+$ T cells after treatment with N6F11 (5 μM), erastin (5 μM), RSL3 (0.5 μM), or Fin56 (5 μM) for 24 hours (*$P < 0.05$; $n = 3$ biologically independent samples; data are presented as mean ± SD).

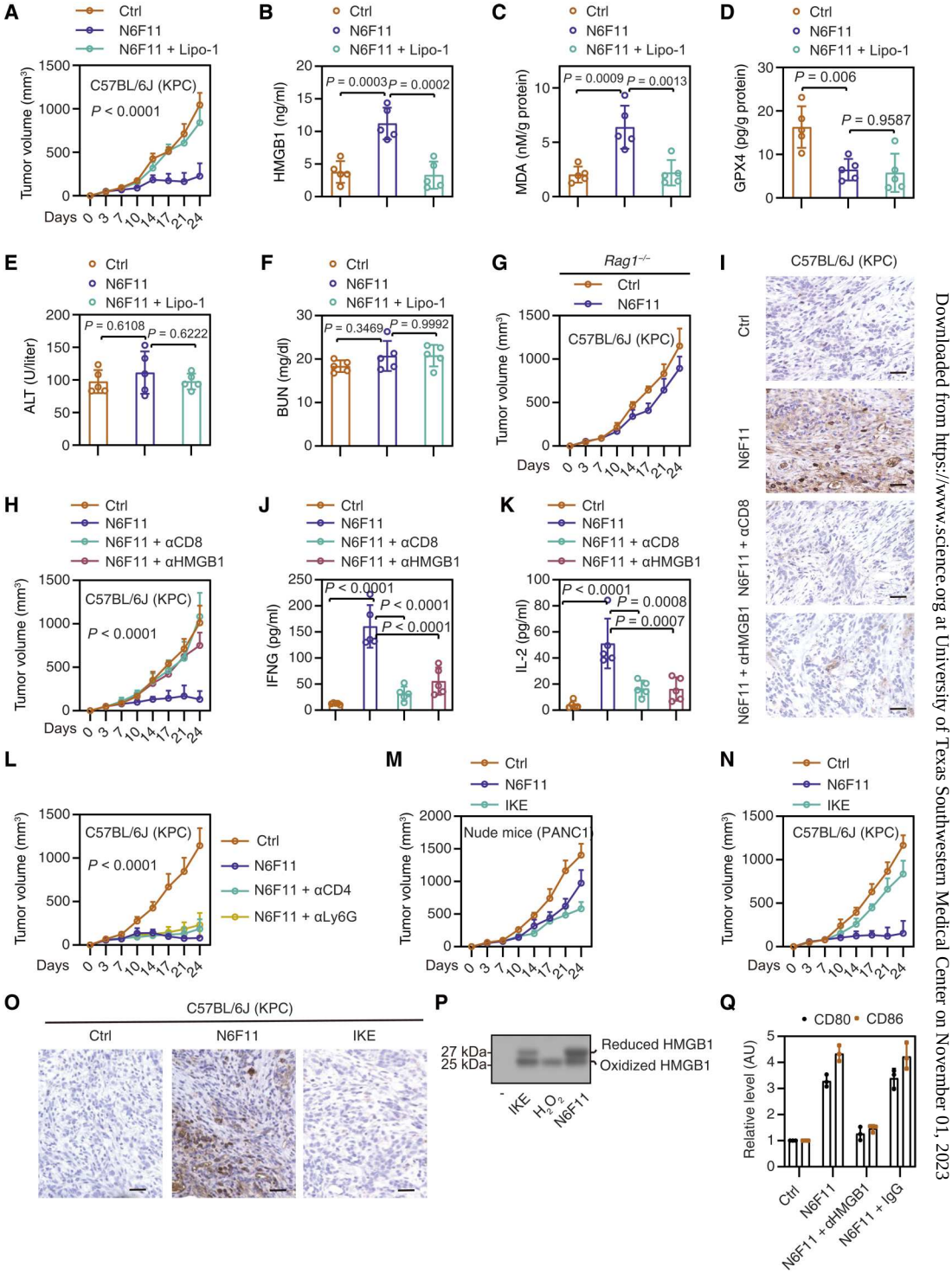

Fig. 7. The therapeutic effect of N6F11 depends on CD8$^+$ T cells and HMGB1. (**A**) C57BL/6 mice were inoculated with 1×10^6 KPC tumor cells and treated with N6F11 (10 mg/kg; days 3, 7, 10, and 14) in the absence or presence of liproxstatin-1 (Lipo-1; 10 mg/kg). Tumor volumes were calculated ($n = 5$ mice per group; two-way ANOVA with Tukey's multiple comparisons test; data are presented as mean ± SD). (**B**) The concentrations of serum HMGB1 at day 24 after tumor inoculation were assayed ($n = 5$ mice per group; one-way ANOVA with Tukey's multiple comparisons test). (**C**) The concentrations of tumor MDA at day 24 after tumor inoculation were assayed ($n = 5$ mice per group; one-way ANOVA with Tukey's multiple comparisons test). (**D**) The concentrations of tumor GPX4 at day 24 after tumor inoculation were assayed ($n = 5$ mice per group; one-way ANOVA with Tukey's multiple comparisons test). (**E**) The concentrations of serum alanine aminotransferase (ALT) at day 24 after tumor inoculation were assayed ($n = 5$ mice per group; one-way ANOVA with Tukey's multiple comparisons test). (**F**) The concentrations of serum blood urea nitrogen (BUN) at day 24 after tumor inoculation were assayed ($n = 5$ mice per group; one-way ANOVA with Tukey's multiple comparisons test). (**G**) *Rag1*$^{-/-}$ mice were inoculated with 1×10^6 KPC tumor cells and treated with N6F11 (3 mg/kg; days 3, 7, 10, and 14). Tumor volumes were calculated ($n = 5$ mice per group; data are presented as mean ± SD). (**H**) C57BL/6 mice were inoculated with 1×10^6 KPC tumor cells and treated with N6F11 (3 mg/kg; days 3, 7, 10, and 14). In addition, 200 μg of anti-CD8 antibodies (αCD8) was administered 1 day before treatment initiation and then twice a week for 3 weeks; anti-HMGB1 antibodies (20 mg/kg; αHMGB1) were administered on days 3, 7, 10, and 14. Tumor volumes were calculated ($n = 5$ mice per group; two-way ANOVA with Tukey's multiple comparisons test; data are presented as mean ± SD). (**I**) Representative immunohistochemistry (IHC) staining of CD8 in tumor at day 24 after tumor inoculation. Scale bars, 50 μm. (**J**) ELISA analysis of serum IFNG at day 24 after tumor inoculation ($n = 5$ mice per group; one-way ANOVA with Tukey's multiple comparisons test; data are presented as mean ± SD). (**K**) ELISA analysis of serum IL-2 at day 24 after tumor inoculation ($n = 5$ mice per group; one-way ANOVA with Tukey's multiple comparisons test; data are presented as mean ± SD). (**L**) C57BL/6 mice were inoculated with 1×10^6 KPC tumor cells and treated with N6F11 (3 mg/kg; days 3, 7, 10, and 14). In addition, 200 μg of anti-CD4–depleting antibody (αCD4) or 500 μg of neutrophil-depleting antibody (αLy6G) was administered 1 day before treatment initiation and then twice a week for 3 weeks; anti-HMGB1 antibodies (20 mg/kg; αHMGB1) were administered on days 3, 7, 10, and 14. Tumor volumes were calculated ($n = 5$ mice per group; two-way ANOVA with Tukey's multiple comparisons test; data are presented as mean ± SD). (**M**) Nude mice were inoculated with 1×10^6 PANC1 tumor cells and treated with N6F11 (10 mg/kg; days 3, 7, 10, and 14) or IKE (30 mg/kg; days 3, 7, 10, and 14). Tumor volumes were calculated ($n = 5$ mice per

Figure caption continued next page

(Figure 7 caption continued) group; data are presented as mean ± SD). (**N**) C57BL/6 mice were inoculated with 1×10^6 KPC tumor cells and treated with N6F11 (10 mg/kg; days 3, 7, 10, and 14) or IKE (30 mg/kg; days 3, 7, 10, and 14). Tumor volumes were calculated ($n = 5$ mice per group; data are presented as mean ± SD). (**O**) Representative IHC staining of CD8 in tumor at day 24 after tumor inoculation. Scale bars, 50 μm. (**P**) Western blot analysis of HMGB1 release in the supernatants of KPC cells treated with IKE (5 μM), H_2O_2 (100 μM), or N6F11 (5 μM) for 12 hours. (**Q**) Anti-HMGB1 antibodies (αHMGB1; 10 mg/ml) inhibited CD80 and CD86 expression in DC2.4 cells in response to N6F11-treated KPC cells for 12 hours ($n = 3$ biologically independent samples; data are presented as mean ± SD).

product of lipid peroxidation (*58*); $P = 0.0009$; Fig. 7C], and decreased tumor GPX4 protein ($P = 0.006$; Fig. 7D). The administration of the ferroptosis inhibitor liproxstatin-1 interfered with N6F11-mediated tumor suppression (Fig. 7A). The function of liver and kidney was not affected by N6F11 (Fig. 7, E and F). Hematoxylin and eosin staining also revealed that N6F11 did not induce any detectable damage to the intestinal or kidney epithelial cells (fig. S7, A and B). However, in *Rag1* knockout ($Rag1^{-/-}$) C57BL/6J mice that cannot produce mature T and B cells, the therapeutic effect of N6F11 was reduced (Fig. 7G), indicating that tumor control in vivo largely requires adaptive immune cells.

Next, we specifically deleted cytotoxic T lymphocytes using anti-mouse CD8α (αCD8) (*59*). $CD8^+$ T cell depletion was sufficient to eliminate the therapeutic effect of N6F11 (Fig. 7, H and I). Because HMGB1 is a mediator of ICD, we also treated the mice with HMGB1-neutralizing antibodies (αHMGB1) (*60*). The αHMGB1 reversed the anticancer activity of N6F11 and decreased the number of tumor-infiltrating $CD8^+$ T cells (Fig. 7, H and I). Serum effector cytokines, such as interferon gamma (IFNG/IFN-γ) and interleukin-2 (IL-2), were increased when tumor-bearing mice were treated with N6F11, and this surge in cytokines was inhibited by the administration of αCD8 or αHMGB1 (Fig. 7, J and K). Unlike αCD8 (Fig. 7H), anti-CD4–depleting antibody (αCD4) or neutrophil-depleting antibody (αLy6G) failed to affect N6F11-induced tumor suppression in C57BL/6J mice (Fig. 7L).

We further compared the anticancer activity of N6F11 with IKE, an erastin analog that is metabolically stable in vivo (*61*). IKE at 30 mg/kg exhibited better anticancer activity than N6F11 at 10 mg/kg in immunocompromised nude mice implanted with human PANC1 cells ($P < 0.0001$; Fig. 7M). However, the anticancer activity of IKE, but not N6F11, was limited in immunocompetent C57BL/6J mice implanted with mouse KPC cells (Fig. 7N). The IKE group had a decrease in tumor-infiltrating $CD8^+$ T cells in C57BL/6J mice (Fig. 7O). These findings suggest that IKE and N6F11 have differential effects on $CD8^+$ cytotoxic T cell infiltration in the tumor microenvironment.

The immune activity of HMGB1 in inflammation and cell death is affected by its redox status (*62*). Typically, reduced HMGB1 exhibits immune activity, whereas oxidized HMGB1 has no immune-stimulatory activity (*63*, *64*). However, oxidized HMGB1 can induce cell death in cancer cells (*65*). We conducted a Western blot assay to investigate the state of released HMGB1 in KPC cells after treatment with N6F11 and IKE. Our data indicated that both N6F11 and IKE can induce HMGB1 release in a mixed state of reduced and oxidized HMGB1 (Fig. 7P). Compared with IKE, N6F11 caused more HMGB1 release in its reduced form (Fig. 7P). As a positive control, H_2O_2 induced the release of HMGB1 in an almost fully oxidized form (Fig. 7P). Analysis of the immunogenicity of N6F11-induced ferroptotic KPC cells, in coculture experiments with murine DCs (DC2.4), revealed an increase in the expression of DC maturation markers, such as the costimulatory molecules CD80 and CD86 (Fig. 7Q). The presence of αHMGB1 inhibited this process, whereas control immunoglobulin G (IgG) had no effect (Fig. 7Q).

The hallmark of an adaptive immune response is the formation of immunological memory that initiates a rapid recall response when the same antigen appears (*66*). To determine whether there was such a memory response, we took advantage of a prophylactic tumor vaccination model (*6*). N6F11-treated KPC cells were injected subcutaneously into the right flanks of immunocompetent female C57BL/6J mice (fig. S8A). One week later, the mice were re-challenged with live KPC cells injected into the opposite flank. We found that N6F11-treated KPC cells protected mice from tumor re-challenge and that this long-distance protection was curtailed by the administration of αCD8 or αHMGB1 (fig. S8B). MC38, a murine colon adenocarcinoma cell line derived from C57BL/6J mice, was also sensitive to N6F11-induced ferroptosis with HMGB1 release (fig. S8, C and D). N6F11-treated MC38 cells also induced protective immunity in the tumor vaccination model (fig. S8E). These findings indicate that N6F11 can suppress tumor growth in a way that induces HMGB1- and $CD8^+$ T cell–dependent immune memory.

Advanced tumors develop an immunosuppressive microenvironment through multiple mechanisms, including the up-regulation of immune checkpoints (*2*). Driven by this consideration, we combined the effects of N6F11 and anti-CD274 antibodies (αCD274) in advanced cancer. Tumors were allowed to reach a size of 150 to 200 mm^3 on day 10 after inoculation and then were treated with N6F11 and αCD274 alone or in combination. Treatment of advanced KPC or MC38 cancers with N6F11 or αCD274 used as stand-alone agents was not statistically significant (fig. S8, F and G). However, the combined administration of N6F11 and αCD274 inhibited tumor growth (fig. S8, F and G). The combined effects of N6F11 and αCD274 were reduced by αCD8 or αHMGB1 antibodies (fig. S8, F and G). The administration of N6F11, but not IKE, combined with αCD274 prolonged (by approximately 2.5 times) the average life expectancy of KPC mice, which develop aggressive pancreatic cancer driven by transgenic *KRAS* and *TP53* mutations (fig. S8H) (*67*). In an orthotopic model of PDAC, where KPC cells were implanted into the pancreas, the combination of N6F11 and αCD274 significantly ($P = 0.0009$) increased the survival of C57BL/6J mice compared with the group that received either treatment alone (fig. S8I).

DISCUSSION

The goal of antineoplastic therapy is to eradicate cancer cells without side effects on normal tissues. Here, we report that N6F11 selectively induces ferroptosis in cancer but not in immune cells, thereby limiting the immunosuppressive side effects of established ferroptosis inducers (*16*–*18*, *68*). This cancer-selective effect is mediated by TRIM25-dependent GPX4 protein degradation. In addition, TRIM25 is a tumor marker associated with poor prognosis (*69*–*73*).

Most drugs now used in clinical oncology trigger cancer cell death by caspase-dependent apoptosis (*74*). However, one of the hallmarks of human cancer is intrinsic or acquired resistance to apoptosis (*75*), a fact that spurred the search for nonapoptotic cell death subroutines that may be ignited to bypass drug resistance. GPX4 is a driver of acquired drug resistance, which prevents a stable and complete response to cancer treatments (*14*). Previous studies attempted to use direct GPX4 inhibitors to kill tumor cells, although at the cost of immunosuppressive side effects (*15*–*17*, *68*). The conditional depletion of *Gpx4* in the murine kidney or liver causes ferroptotic damage, underscoring the probable side effects of direct pharmacological GPX4 inhibition (*76*, *77*). Here, we demonstrated the effectiveness and safety of an indirect strategy of GPX4 inhibition that involves an N6F11-elicited, TRIM25-dependent degradation of GPX4 protein by the UPS. This strategy does not cause ferroptosis of DCs, $CD8^+$ T, NK, and neutrophil cells, and N6F11 did not elicit detectable damage to the liver, kidney, or intestines.

Our discovery of N6F11 as a TRIM25 activator reveals an actionable drug target that is highly expressed in many cancer types (*69*–*73*). Future studies must determine whether N6F11 will lead a new class of successful TRIM25 activators or whether computer-designed high-throughput screens will result in the discovery of even more advantageous lead compounds targeting TRIM25. N6F11 treatment for 1 hour did not cause GPX4 protein degradation but increased the interaction between GPX4 and TRIM25, indicating that the degradation process of GPX4 protein is a dynamic multistage process.

The most successful cancer drugs induce clinically relevant antitumor immune responses, which obviously depend on the antigenicity of cancer cells and on their ability to generate innate sensor signals (*78*). Immunogenic cancer cell death is accompanied by the exposure and release of DAMPs, facilitating the recruitment and activation of DCs, the presentation of tumor-associated antigens by DCs to cytotoxic T lymphocytes, and the consequent anticancer immune response (*79*). We observed that HMGB1 is a mediator of N6F11-induced ICD and hence contributes to the induction of an adaptive immune response. HMGB1 is not only passively released from damaged cells but can also be actively secreted from activated immune cells, suggesting that it amplifies cell death–related immune responses (*80*). Given that we observed the release of both reduced and oxidized forms of HMGB1 after N6F11 treatment, further research is needed to address the potential immune side effects associated with oxidized HMGB1 (*81*–*83*).

Although checkpoint blockade, especially PDCD1 or CD274 blockade, has achieved great clinical success, few patients exhibit durable therapeutic responses from it (*84*). We demonstrated that the combined administration of N6F11 and anti-CD274 has a synergistic effect in advanced tumors, further enhancing HMGB1-dependent cytotoxic T cell responses. As a metaphor describing the interaction between immunotherapy and cytotoxicants (*85*), one might state that CD274 blockade revitalizes the adaptive immune response by "releasing the brakes," whereas N6F11 elicits an HMGB1-dependent innate signal by "adding fuel."

An important limitation of our study is that although we have shown GPX4 to be a substrate of TRIM25 in response to N6F11, it is possible that other, as-yet-unknown substrates also contribute to the TRIM25-dependent regulation of ferroptosis. We demonstrated that N6F11 promotes TRIM25-mediated selective ubiquitination of GPX4, but the compound does not interact directly with GPX4. Although we determined that a single chloride group is responsible for the ferroptosis-inducing activity of N6F11 and that the RING domain of TRIM25 is the binding site of N6F11 in cancer cells, a deeper structure-activity relationship between N6F11 and TRIM25 requires additional experimental evidence, such as cryo-electron microscopy reconstructions.

In summary, we identified a small molecule, N6F11, that induces the selective degradation of GPX4 in malignant, but not immune, cells through the direct activation of TRIM25. In small tumors, N6F11-induced ferroptosis initiates a powerful antitumor immune system. In advanced tumors, especially genetically engineered mutant *KRAS/TP53*-driven PDAC models, N6F11, but not IKE, can be advantageously combined with CD274-targeted immunotherapy. We expect that such an approach warrants further preclinical evaluation for its possible incorporation into the oncological armamentarium.

MATERIALS AND METHODS

Study design

Our study aimed to identify small molecular compounds that selectively target the GPX4 pathway in cancer cells while leaving immune cells unaffected, as a potential treatment for cancer. Through a screen of a small molecular library, we identified N6F11 as the top inducer of GPX4 protein degradation in cancer cells. We further elucidated the molecular mechanism by which N6F11 promotes GPX4 protein degradation through TRIM25. In addition, we evaluated the safety and efficacy of N6F11 in managing tumor growth in mice. In all experiments, animals were randomly assigned to different treatment groups without blinding, and sample sizes are specified in each figure legend. No samples or animals were excluded from our analyses. For every figure, appropriate statistical tests were applied, and all data met the assumptions of these tests. Although we did not use statistical methods to predetermine sample sizes, our sample sizes are consistent with those commonly used in the field. Details of all reagents used in the study are provided in table S1.

Cell culture and treatment

Human or mouse cancer cell lines were obtained from the American Type Culture Collection or collaborators (table S1). $Atg5^{-/-}$ and $Atg7^{-/-}$ MEFs were gifts from N. Mizushima. $Ripk3^{-/-}$ MEFs were gifts from D. R. Green. Primary immune cells were obtained from STEMCELL Technologies. DC2.4 cells were purchased from MilliporeSigma. Cells were cultured in Dulbecco's modified Eagle's medium (Thermo Fisher Scientific, 11995073) or RPMI 1640 (Thermo Fisher Scientific, 11875119) supplemented with 10% heat-inactivated fetal bovine serum (Millipore, TMS-013-B) and 1% penicillin and streptomycin (Thermo Fisher Scientific, 15070-063) at 37°C, 95% humidity, and 5% CO_2. Transwell inserts (Thermo Fisher Scientific, 140620) with a pore size of 0.4 μm on a 24-well culture plate were used to assess the impact of ferroptotic KPC cells on DC2.4 cells (*86*). All cells were mycoplasma free and authenticated using short tandem repeat DNA profiling analysis.

Dimethyl sulfoxide (DMSO) was used to prepare the stock solution of drugs. The final concentration of DMSO in the drug working solution in the cells was <0.01%. DMSO of 0.01% was

used as a vehicle control in all cell culture assays. N6F11 and its analogs were synthesized by WuXi AppTec.

Drug screening

A commercial library of 4208 synthetic compounds of unknown biological activity was purchased from Selleck Chemicals. We treated 1×10^4 PANC1 cells with compound (5 μM) for 24 hours in each well of a 96-well plate. After fixation, permeabilization, and unspecific binding blocking (5% milk; Cell Signaling Technology, 9999), cells were stained with anti-GPX4 (1:1000) and anti-ACTB antibodies (1:1000) followed by DyLight-conjugated secondary antibodies (1:2000; Cell Signaling Technology, 5366 and 5257). Images were acquired and analyzed by an Odyssey Imaging System (LI-COR Biosciences). After measuring the ratio of the red signal (700 nm) of GPX4 and the green signal (800 nm) of ACTB, the top candidates were further examined by traditional Western blot analysis.

Generation of 3D spheroids

A total of 1.5×10^3 cells (PANC1 or MiaPACA2) were mixed in 20 μl of Matrigel (Sigma-Aldrich, CLS354277) and planted in each well in a 48-well plate. Plates were incubated for 5 days at 37°C, 5% CO_2, 95% humidity for formation of spheroids of cells. After that, spheroids were treated with N6F11 in fresh medium for the indicated time and concentrations. Subsequently, spheroid images were acquired using a EVOS Cell Imaging System (Thermo Fisher Scientific).

Animal model

We conducted all animal care and experiments in accordance with the Association for Assessment and Accreditation of Laboratory Animal Care guidelines and with approval from our institutional animal care and use committees [University of Texas Southwestern Medical Center (#102605) and Guangzhou Medical University (#9729)]. All mice were housed under a 12-hour light-dark diurnal cycle with controlled temperature (20° to 25°C) and relative humidity (40 to 60%). Food and water were available ad libitum. Experiments were carried out under pathogen-free conditions, and the health status of mouse lines was routinely checked by veterinary staff. No wild animals were used in the study. Experiments were carried out with randomly chosen littermates of the same sex and matched by age and body weight. Animals were euthanized at the indicated time by CO_2 asphyxia, and blood samples and tissue were collected.

To generate murine subcutaneous tumors, wild-type C57BL/6J mice or nude mice [8 to 10 weeks old, 22 to 26 g in weight, and female or male (1:1)] were inoculated with 1×10^6 KPC or PANC1 tumor cells and treated with N6F11 (10 mg/kg; days 3, 7, 10, and 14) or IKE (30 mg/kg; days 3, 7, 10, and 14) in the absence or presence of liproxstatin-1 (10 mg/kg). *Rag1*$^{-/-}$ mice on a C57BL/6J background were used as a control. To deplete immune cells, 200 μg of anti-CD8–depleting antibodies (clone 2.43, BioXcell, BE0061), 200 μg of anti-CD4–depleting antibodies (clone GK1.5, BioXcell, BE0003-1), or 500 μg of neutrophil-depleting antibodies (αLy6G; clone 1A8, BioXcell, BE0075-1) was administered 1 day before treatment initiation and then twice a week for 3 weeks. To determine the role of HMGB1 in mediating antitumor immunity, anti-HMGB1 monoclonal antibodies [20 mg/kg; clone 2G7 (*87*)] were administered on days 3, 7, 10, and 14. N6F11, IKE, and all antibodies were administered to mice through intraperitoneal injection. Tumors were measured twice weekly, and volumes were calculated using the formula length × width^2 × π/6.

For advanced tumor treatment, C57BL/6J mice [8 to 10 weeks old, 22 to 26 g in weight, and female or male (1:1)] were inoculated with 1×10^6 KPC or MC38 tumor cells to reach 150 to 200 mm^3 at day 10 and then treated with N6F11 (10 mg/kg; days 10, 14, and 17). A total of 20 mg/kg of anti-CD274 antibodies (clone 10F.9G2, BioLegend, 124318) or anti-HMGB1 antibodies was administered on days 10, 14, and 17. In addition, 200 μg of anti-CD8 antibodies was administered 1 day before treatment initiation and then twice a week for 3 weeks. Tumors were measured twice weekly, and volumes were calculated using the formula length × width^2 × π/6.

To generate a tumor vaccination model, a total of 5×10^6 KPC or MC38 cells, untreated or treated with either N6F11 (5 μM; 24 hours), were inoculated subcutaneously in 200 μl of phosphate-buffered saline (PBS) into the lower flanks of C57BL/6J mice [8 to 10 weeks old, 22 to 26 g in weight, and female or male (1:1)], whereas 5×10^5 untreated control cells were inoculated into the contralateral flank 7 days later (*88*). The percentage of tumor-free mice was monitored every week for 6 weeks.

Pdx1-Cre;*K-Ras*$^{G12D/+}$;*Tp53*$^{R172H/+}$ mice (KPC) were produced as previously described (*67*). At 1 month of age, female or male (1:1) mice were randomly allocated into groups and then treated (intraperitoneally) with control IgG or anti-CD274 antibodies (20 mg/kg) in the absence or presence of N6F11 (10 mg/kg) or IKE (30 mg/kg) for 8 weeks (twice a week for the first 4 weeks and then once a week). Animal survival was monitored every week.

To generate orthotopic tumors, female or male (1:1) C57BL/6 mice were surgically implanted with 5×10^5 KPC cells in 10 μl of PBS into the tail of the pancreas. One week after implantation, mice were randomly assigned to groups and treated with anti-CD274 antibodies (20 mg/kg) alone or in combination with N6F11 (10 mg/kg) for 4 weeks, with treatments administered twice a week. Mouse survival was monitored weekly.

Bioinformatics analysis

A protein-protein interaction database (http://iid.ophid.utoronto.ca/#analyze_PPIs) was used to assay GPX4-binding protein. Prediction of Ubiquitination Sites with Bayesian Discriminant Method (BDM-PUB) (http://bdmpub.biocuckoo.org/results.php) was used to assay the potential ubiquitination site on GPX4. Online molecular docking software (https://playmolecule.com/BindScope/) was used to assay the possible binding between N6F11 and TRIM25. The Human Protein Atlas (https://proteinatlas.org/) was used to assay the expression of TRIM25 in different cells.

Statistical analysis

Data are presented as mean ± SD except where otherwise indicated. GraphPad Prism (version 8.4.3) was used to collect and analyze data. Unpaired Student's *t* tests were used to compare the means of two groups. A one-way (for one independent variable) or two-way (for two independent variables) analysis of variance (ANOVA) with Tukey's multiple comparisons test was used for comparison among the different groups on all pairwise combinations. Log-rank tests were used to compare differences in mortality rates between groups. A P value of <0.05 was considered statistically significant. The exact value of n within the figures and replicates is indicated in the figure legends.

Supplementary Materials

This PDF file includes:
Materials and Methods
Figs. S1 to S8
Tables S1 and S2
References (*89*–*94*)

Other Supplementary Material for this manuscript includes the following:
Data file S1
MDAR Reproducibility Checklist

REFERENCES AND NOTES

1. S. P. Kubli, T. Berger, D. V. Araujo, L. L. Siu, T. W. Mak, Beyond immune checkpoint blockade: Emerging immunological strategies. *Nat. Rev. Drug Discov.* **20**, 899–919 (2021).
2. A. Ribas, J. D. Wolchok, Cancer immunotherapy using checkpoint blockade. *Science* **359**, 1350–1355 (2018).
3. A. Kalbasi, A. Ribas, Tumour-intrinsic resistance to immune checkpoint blockade. *Nat. Rev. Immunol.* **20**, 25–39 (2020).
4. A. J. Schoenfeld, M. D. Hellmann, Acquired resistance to immune checkpoint inhibitors. *Cancer Cell* **37**, 443–455 (2020).
5. C. V. Rothlin, S. Ghosh, Lifting the innate immune barriers to antitumor immunity. *J. Immunother. Cancer* **8**, e000695 (2020).
6. L. Apetoh, F. Ghiringhelli, A. Tesniere, M. Obeid, C. Ortiz, A. Criollo, G. Mignot, M. C. Maiuri, E. Ullrich, P. Saulnier, H. Yang, S. Amigorena, B. Ryffel, F. J. Barrat, P. Saftig, F. Levi, R. Lidereau, C. Nogues, J. P. Mira, A. Chompret, V. Joulin, F. Clavel-Chapelon, J. Bourhis, F. Andre, S. Delaloge, T. Tursz, G. Kroemer, L. Zitvogel, Toll-like receptor 4-dependent contribution of the immune system to anticancer chemotherapy and radiotherapy. *Nat. Med.* **13**, 1050–1059 (2007).
7. L. Galluzzi, J. Humeau, A. Buque, L. Zitvogel, G. Kroemer, Immunostimulation with chemotherapy in the era of immune checkpoint inhibitors. *Nat. Rev. Clin. Oncol.* **17**, 725–741 (2020).
8. S. J. Dixon, K. M. Lemberg, M. R. Lamprecht, R. Skouta, E. M. Zaitsev, C. E. Gleason, D. N. Patel, A. J. Bauer, A. M. Cantley, W. S. Yang, B. Morrison III, B. R. Stockwell, Ferroptosis: An iron-dependent form of nonapoptotic cell death. *Cell* **149**, 1060–1072 (2012).
9. W. S. Yang, R. SriRamaratnam, M. E. Welsch, K. Shimada, R. Skouta, V. S. Viswanathan, J. H. Cheah, P. A. Clemons, A. F. Shamji, C. B. Clish, L. M. Brown, A. W. Girotti, V. W. Cornish, S. L. Schreiber, B. R. Stockwell, Regulation of ferroptotic cancer cell death by GPX4. *Cell* **156**, 317–331 (2014).
10. Y. Xie, W. Hou, X. Song, Y. Yu, J. Huang, X. Sun, R. Kang, D. Tang, Ferroptosis: Process and function. *Cell Death Differ.* **23**, 369–379 (2016).
11. I. Efimova, E. Catanzaro, L. Van der Meeren, V. D. Turubanova, H. Hammad, T. A. Mishchenko, M. V. Vedunova, C. Fimognari, C. Bachert, F. Coppieters, S. Lefever, A. G. Skirtach, O. Krysko, D. V. Krysko, Vaccination with early ferroptotic cancer cells induces efficient antitumor immunity. *J. Immunother. Cancer* **8**, e001369 (2020).
12. W. Wang, M. Green, J. E. Choi, M. Gijon, P. D. Kennedy, J. K. Johnson, P. Liao, X. Lang, I. Kryczek, A. Sell, H. Xia, J. Zhou, G. Li, J. Li, W. Li, S. Wei, L. Vatan, H. Zhang, W. Szeliga, W. Gu, R. Liu, T. S. Lawrence, C. Lamb, Y. Tanno, M. Cieslik, E. Stone, G. Georgiou, T. A. Chan, A. Chinnaiyan, W. Zou, $CD8^+$ T cells regulate tumour ferroptosis during cancer immunotherapy. *Nature* **569**, 270–274 (2019).
13. L. Jiang, N. Kon, T. Li, S. J. Wang, T. Su, H. Hibshoosh, R. Baer, W. Gu, Ferroptosis as a p53-mediated activity during tumour suppression. *Nature* **520**, 57–62 (2015).
14. M. J. Hangauer, V. S. Viswanathan, M. J. Ryan, D. Bole, J. K. Eaton, A. Matov, J. Galeas, H. D. Dhruv, M. E. Berens, S. L. Schreiber, F. McCormick, M. T. McManus, Drug-tolerant persister cancer cells are vulnerable to GPX4 inhibition. *Nature* **551**, 247–250 (2017).
15. L. Han, L. Bai, C. Qu, E. Dai, J. Liu, R. Kang, D. Zhou, D. Tang, Y. Zhao, PPARG-mediated ferroptosis in dendritic cells limits antitumor immunity. *Biochem. Biophys. Res. Commun.* **576**, 33–39 (2021).
16. X. Ma, L. Xiao, L. Liu, L. Ye, P. Su, E. Bi, Q. Wang, M. Yang, J. Qian, Q. Yi, CD36-mediated ferroptosis dampens intratumoral $CD8^+$ T cell effector function and impairs their antitumor ability. *Cell Metab.* **33**, 1001–1012.e5 (2021).
17. S. Xu, O. Chaudhary, P. Rodriguez-Morales, X. Sun, D. Chen, R. Zappasodi, Z. Xu, A. F. M. Pinto, A. Williams, I. Schulze, Y. Farsakoglu, S. K. Varanasi, J. S. Low, W. Tang, H. Wang, B. McDonald, V. Tripple, M. Downes, R. M. Evans, N. A. Abumrad, T. Merghoub, J. D. Wolchok, M. N. Shokhirev, P. C. Ho, J. L. Witztum, B. Emu, G. Cui, S. M. Kaech, Uptake of oxidized lipids by the scavenger receptor CD36 promotes lipid peroxidation and dysfunction in $CD8^+$ T cells in tumors. *Immunity* **54**, 1561–1577.e7 (2021).
18. R. Kim, A. Hashimoto, N. Markosyan, V. A. Tyurin, Y. Y. Tyurina, G. Kar, S. Fu, M. Sehgal, L. Garcia-Gerique, A. Kossenkov, B. A. Gebregziabher, J. W. Tobias, K. Hicks, R. A. Halpin, N. Cvetesic, H. Deng, L. Donthireddy, A. Greenberg, B. Nam, R. H. Vonderheide, Y. Nefedova, V. E. Kagan, D. I. Gabrilovich, Ferroptosis of tumour neutrophils causes immune suppression in cancer. *Nature* **612**, 338–346 (2022).
19. X. Chen, R. Kang, G. Kroemer, D. Tang, Broadening horizons: The role of ferroptosis in cancer. *Nat. Rev. Clin. Oncol.* **18**, 280–296 (2021).
20. X. Chen, J. Li, R. Kang, D. J. Klionsky, D. Tang, Ferroptosis: Machinery and regulation. *Autophagy* **17**, 2054–2081 (2021).
21. Z. Wu, Y. Geng, X. Lu, Y. Shi, G. Wu, M. Zhang, B. Shan, H. Pan, J. Yuan, Chaperone-mediated autophagy is involved in the execution of ferroptosis. *Proc. Natl. Acad. Sci. U.S.A.* **116**, 2996–3005 (2019).
22. S. Zhu, Q. Zhang, X. Sun, H. J. Zeh III, M. T. Lotze, R. Kang, D. Tang, HSPA5 regulates ferroptotic cell death in cancer cells. *Cancer Res.* **77**, 2064–2077 (2017).
23. K. Shimada, R. Skouta, A. Kaplan, W. S. Yang, M. Hayano, S. J. Dixon, L. M. Brown, C. A. Valenzuela, A. J. Wolpaw, B. R. Stockwell, Global survey of cell death mechanisms reveals metabolic regulation of ferroptosis. *Nat. Chem. Biol.* **12**, 497–503 (2016).
24. J. K. Eaton, L. Furst, R. A. Ruberto, D. Moosmayer, A. Hilpmann, M. J. Ryan, K. Zimmermann, L. L. Cai, M. Niehues, V. Badock, A. Kramm, S. Chen, R. C. Hillig, P. A. Clemons, S. Gradl, C. Montagnon, K. E. Lazarski, S. Christian, B. Bajrami, R. Neuhaus, A. L. Eheim, V. S. Viswanathan, S. L. Schreiber, Selective covalent targeting of GPX4 using masked nitrile-oxide electrophiles. *Nat. Chem. Biol.* **16**, 497–506 (2020).
25. V. Boveia, A. Schutz-Geschwender, Quantitative analysis of signal transduction with In-Cell Western immunofluorescence assays. *Methods Mol. Biol.* **1314**, 115–130 (2015).
26. J. Liu, X. Song, F. Kuang, Q. Zhang, Y. Xie, R. Kang, G. Kroemer, D. Tang, NUPR1 is a critical repressor of ferroptosis. *Nat. Commun.* **12**, 647 (2021).
27. Y. Xie, R. Kang, D. J. Klionsky, D. Tang, GPX4 in cell death, autophagy, and disease. *Autophagy* **19**, 2621–2638 (2023).
28. Q. Ran, H. Liang, Y. Ikeno, W. Qi, T. A. Prolla, L. J. Roberts II, N. Wolf, H. Van Remmen, A. Richardson, Reduction in glutathione peroxidase 4 increases life span through increased sensitivity to apoptosis. *J. Gerontol. A Biol. Sci. Med. Sci.* **62**, 932–942 (2007).
29. O. Canli, Y. B. Alankus, S. Grootjans, N. Vegi, L. Hultner, P. S. Hoppe, T. Schroeder, P. Vandenabeele, G. W. Bornkamm, F. R. Greten, Glutathione peroxidase 4 prevents necroptosis in mouse erythroid precursors. *Blood* **127**, 139–148 (2016).
30. R. Kang, L. Zeng, S. Zhu, Y. Xie, J. Liu, Q. Wen, L. Cao, M. Xie, Q. Ran, G. Kroemer, H. Wang, T. R. Billiar, J. Jiang, D. Tang, Lipid peroxidation drives gasdermin D-mediated pyroptosis in lethal polymicrobial sepsis. *Cell Host Microbe* **24**, 97–108.e4 (2018).
31. K. Azuma, T. Koumura, R. Iwamoto, M. Matsuoka, R. Terauchi, S. Yasuda, T. Shiraya, S. Watanabe, M. Aihara, H. Imai, T. Ueta, Mitochondrial glutathione peroxidase 4 is indispensable for photoreceptor development and survival in mice. *J. Biol. Chem.* **298**, 101824 (2022).
32. Q. Wen, J. Liu, R. Kang, B. Zhou, D. Tang, The release and activity of HMGB1 in ferroptosis. *Biochem. Biophys. Res. Commun.* **510**, 278–283 (2019).
33. X. Sun, Z. Ou, R. Chen, X. Niu, D. Chen, R. Kang, D. Tang, Activation of the p62-Keap1-NRF2 pathway protects against ferroptosis in hepatocellular carcinoma cells. *Hepatology* **63**, 173–184 (2016).
34. F. Kuang, J. Liu, Y. Xie, D. Tang, R. Kang, MGST1 is a redox-sensitive repressor of ferroptosis in pancreatic cancer cells. *Chem. Biol.* **28**, 765–775.e5 (2021).
35. S. J. Dixon, D. N. Patel, M. Welsch, R. Skouta, E. D. Lee, M. Hayano, A. G. Thomas, C. E. Gleason, N. P. Tatonetti, B. S. Slusher, B. R. Stockwell, Pharmacological inhibition of cystine-glutamate exchange induces endoplasmic reticulum stress and ferroptosis. *eLife* **3**, e02523 (2014).
36. X. Chen, X. Song, J. Li, R. Zhang, C. Yu, Z. Zhou, J. Liu, S. Liao, D. J. Klionsky, G. Kroemer, J. Liu, D. Tang, R. Kang, Identification of HPCAL1 as a specific autophagy receptor involved in ferroptosis. *Autophagy* **19**, 54–74 (2023).
37. W. Hou, Y. Xie, X. Song, X. Sun, M. T. Lotze, H. J. Zeh III, R. Kang, D. Tang, Autophagy promotes ferroptosis by degradation of ferritin. *Autophagy* **12**, 1425–1428 (2016).
38. J. Liu, Y. Liu, Y. Wang, C. Li, Y. Xie, D. J. Klionsky, R. Kang, D. Tang, TMEM164 is a new determinant of autophagy-dependent ferroptosis. *Autophagy* **19**, 945–956 (2023).
39. M. Gao, P. Monian, Q. Pan, W. Zhang, J. Xiang, X. Jiang, Ferroptosis is an autophagic cell death process. *Cell Res.* **26**, 1021–1032 (2016).
40. B. Yan, Y. Ai, Q. Sun, Y. Ma, Y. Cao, J. Wang, Z. Zhang, X. Wang, Membrane damage during ferroptosis is caused by oxidation of phospholipids catalyzed by the oxidoreductases POR and CYB5R1. *Mol. Cell* **81**, 355–369.e10 (2021).
41. Y. Zou, H. Li, E. T. Graham, A. A. Deik, J. K. Eaton, W. Wang, G. Sandoval-Gomez, C. B. Clish, J. G. Doench, S. L. Schreiber, Cytochrome P450 oxidoreductase contributes to phospholipid peroxidation in ferroptosis. *Nat. Chem. Biol.* **16**, 302–309 (2020).
42. K. Bersuker, J. M. Hendricks, Z. Li, L. Magtanong, B. Ford, P. H. Tang, M. A. Roberts, B. Tong, T. J. Maimone, R. Zoncu, M. C. Bassik, D. K. Nomura, S. J. Dixon, J. A. Olzmann, The CoQ

oxidoreductase FSP1 acts parallel to GPX4 to inhibit ferroptosis. *Nature* **575**, 688–692 (2019).
43. S. Doll, F. P. Freitas, R. Shah, M. Aldrovandi, M. C. da Silva, I. Ingold, A. G. Grocin, T. N. X. da Silva, E. Panzilius, C. H. Scheel, A. Mourao, K. Buday, M. Sato, J. Wanninger, T. Vignane, V. Mohana, M. Rehberg, A. Flatley, A. Schepers, A. Kurz, D. White, M. Sauer, M. Sattler, E. W. Tate, W. Schmitz, A. Schulze, V. O'Donnell, B. Proneth, G. M. Popowicz, D. A. Pratt, J. P. F. Angeli, M. Conrad, FSP1 is a glutathione-independent ferroptosis suppressor. *Nature* **575**, 693–698 (2019).
44. E. Dai, W. Zhang, D. Cong, R. Kang, J. Wang, D. Tang, AIFM2 blocks ferroptosis independent of ubiquinol metabolism. *Biochem. Biophys. Res. Commun.* **523**, 966–971 (2020).
45. Y. Xie, S. Zhu, X. Song, X. Sun, Y. Fan, J. Liu, M. Zhong, H. Yuan, L. Zhang, T. R. Billiar, M. T. Lotze, H. J. Zeh III, R. Kang, G. Kroemer, D. Tang, The tumor suppressor p53 limits ferroptosis by blocking DPP4 activity. *Cell Rep.* **20**, 1692–1704 (2017).
46. Y. Yu, Y. Xie, L. Cao, L. Yang, M. Yang, M. T. Lotze, H. J. Zeh, R. Kang, D. Tang, The ferroptosis inducer erastin enhances sensitivity of acute myeloid leukemia cells to chemotherapeutic agents. *Mol. Cell. Oncol.* **2**, e1054549 (2015).
47. F. Chen, X. Cai, R. Kang, J. Liu, D. Tang, Autophagy-dependent ferroptosis in cancer. *Antioxid. Redox Signal.* **39**, 79–101 (2023).
48. Q. P. Dou, J. A. Zonder, Overview of proteasome inhibitor-based anti-cancer therapies: Perspective on bortezomib and second generation proteasome inhibitors versus future generation inhibitors of ubiquitin-proteasome system. *Curr. Cancer Drug Targets* **14**, 517–536 (2014).
49. P. Mei, F. Xie, J. Pan, S. Wang, W. Gao, R. Ge, B. Gao, S. Gao, X. Chen, Y. Wang, J. Wu, C. Ding, J. Li, E3 ligase TRIM25 ubiquitinates RIP3 to inhibit TNF induced cell necrosis. *Cell Death Differ.* **28**, 2888–2899 (2021).
50. Y. Xie, S. Zhu, M. Zhong, M. Yang, X. Sun, J. Liu, G. Kroemer, M. Lotze, H. J. Zeh III, R. Kang, D. Tang, Inhibition of aurora kinase a induces necroptosis in pancreatic carcinoma. *Gastroenterology* **153**, 1429–1443.e5 (2017).
51. I. Ingold, C. Berndt, S. Schmitt, S. Doll, G. Poschmann, K. Buday, A. Roveri, X. Peng, F. Porto Freitas, T. Seibt, L. Mehr, M. Aichler, A. Walch, D. Lamp, M. Jastroch, S. Miyamoto, W. Wurst, F. Ursini, E. S. J. Arner, N. Fradejas-Villar, U. Schweizer, H. Zischka, J. P. Friedmann Angeli, M. Conrad, Selenium utilization by GPX4 is required to prevent hydroperoxide-induced ferroptosis. *Cell* **172**, 409–422.e21 (2018).
52. P. Scheerer, A. Borchert, N. Krauss, H. Wessner, C. Gerth, W. Hohne, H. Kuhn, Structural basis for catalytic activity and enzyme polymerization of phospholipid hydroperoxide glutathione peroxidase-4 (GPx4). *Biochemistry* **46**, 9041–9049 (2007).
53. M. U. Gack, Y. C. Shin, C. H. Joo, T. Urano, C. Liang, L. Sun, O. Takeuchi, S. Akira, Z. Chen, S. Inoue, J. U. Jung, TRIM25 RING-finger E3 ubiquitin ligase is essential for RIG-I-mediated antiviral activity. *Nature* **446**, 916–920 (2007).
54. G. Meroni, G. Diez-Roux, TRIM/RBCC, a novel class of 'single protein RING finger' E3 ubiquitin ligases. *Bioessays* **27**, 1147–1157 (2005).
55. Y. Liu, S. Tao, L. Liao, Y. Li, H. Li, Z. Li, L. Lin, X. Wan, X. Yang, L. Chen, TRIM25 promotes the cell survival and growth of hepatocellular carcinoma through targeting Keap1-Nrf2 pathway. *Nat. Commun.* **11**, 348 (2020).
56. Y. Liu, K. Liu, Y. Huang, M. Sun, Q. Tian, S. Zhang, Y. Qin, TRIM25 promotes TNF-α–induced NF-κB activation through potentiating the K63-linked ubiquitination of TRAF2. *J. Immunol.* **204**, 1499–1507 (2020).
57. J. G. Sanchez, J. J. Chiang, K. M. J. Sparrer, S. L. Alam, M. Chi, M. D. Roganowicz, B. Sankaran, M. U. Gack, O. Pornillos, Mechanism of TRIM25 catalytic activation in the antiviral RIG-I pathway. *Cell Rep.* **16**, 1315–1325 (2016).
58. X. Chen, P. B. Comish, D. Tang, R. Kang, Characteristics and biomarkers of ferroptosis. *Front. Cell Dev. Biol.* **9**, 637162 (2021).
59. K. Liu, J. Huang, J. Liu, C. Li, G. Kroemer, D. Tang, R. Kang, HSP90 mediates IFNγ-induced adaptive resistance to anti-PD-1 immunotherapy. *Cancer Res.* **82**, 2003–2018 (2022).
60. R. Kang, Q. Zhang, W. Hou, Z. Yan, R. Chen, J. Bonaroti, P. Bansal, T. R. Billiar, A. Tsung, Q. Wang, D. L. Bartlett, D. C. Whitcomb, E. B. Chang, X. Zhu, H. Wang, B. Lu, K. J. Tracey, L. Cao, X. G. Fan, M. T. Lotze, H. J. Zeh III, D. Tang, Intracellular Hmgb1 inhibits inflammatory nucleosome release and limits acute pancreatitis in mice. *Gastroenterology* **146**, 1097–1107.e8 (2014).
61. Y. Zhang, H. Tan, J. D. Daniels, F. Zandkarimi, H. Liu, L. M. Brown, K. Uchida, O. A. O'Connor, B. R. Stockwell, Imidazole ketone erastin induces ferroptosis and slows tumor growth in a mouse lymphoma model. *Chem. Biol.* **26**, 623–633.e9 (2019).
62. D. Tang, R. Kang, H. J. Zeh, M. T. Lotze, The multifunctional protein HMGB1: 50 years of discovery. *Nat. Rev. Immunol.*, (2023).
63. E. Venereau, M. Casalgrandi, M. Schiraldi, D. J. Antoine, A. Cattaneo, F. De Marchis, J. Liu, A. Antonelli, A. Preti, L. Raeli, S. S. Shams, H. Yang, L. Varani, U. Andersson, K. J. Tracey, A. Bachi, M. Uguccioni, M. E. Bianchi, Mutually exclusive redox forms of HMGB1 promote cell recruitment or proinflammatory cytokine release. *J. Exp. Med.* **209**, 1519–1528 (2012).
64. H. Yang, H. Wang, Z. Ju, A. A. Ragab, P. Lundback, W. Long, S. I. Valdes-Ferrer, M. He, J. P. Pribis, J. Li, B. Lu, D. Gero, C. Szabo, D. J. Antoine, H. E. Harris, D. T. Golenbock, J. Meng, J. Roth, S. S. Chavan, U. Andersson, T. R. Billiar, K. J. Tracey, Y. Al-Abed, MD-2 is required for disulfide HMGB1-dependent TLR4 signaling. *J. Exp. Med.* **212**, 5–14 (2015).
65. D. Tang, R. Kang, C. W. Cheh, K. M. Livesey, X. Liang, N. E. Schapiro, R. Benschop, L. J. Sparvero, A. A. Amoscato, K. J. Tracey, H. J. Zeh, M. T. Lotze, HMGB1 release and redox regulates autophagy and apoptosis in cancer cells. *Oncogene* **29**, 5299–5310 (2010).
66. M. G. Netea, J. Dominguez-Andres, L. B. Barreiro, T. Chavakis, M. Divangahi, E. Fuchs, L. A. B. Joosten, J. W. M. van der Meer, M. M. Mhlanga, W. J. M. Mulder, N. P. Riksen, A. Schlitzer, J. L. Schultze, C. Stabell Benn, J. C. Sun, R. J. Xavier, E. Latz, Defining trained immunity and its role in health and disease. *Nat. Rev. Immunol.* **20**, 375–388 (2020).
67. S. R. Hingorani, L. Wang, A. S. Multani, C. Combs, T. B. Deramaudt, R. H. Hruban, A. K. Rustgi, S. Chang, D. A. Tuveson, Trp53R172H and KrasG12D cooperate to promote chromosomal instability and widely metastatic pancreatic ductal adenocarcinoma in mice. *Cancer Cell* **7**, 469–483 (2005).
68. B. Wiernicki, S. Maschalidi, J. Pinney, S. Adjemian, T. Vanden Berghe, K. S. Ravichandran, P. Vandenabeele, Cancer cells dying from ferroptosis impede dendritic cell-mediated anti-tumor immunity. *Nat. Commun.* **13**, 3676 (2022).
69. S. Zhou, J. Peng, L. Xiao, C. Zhou, Y. Fang, Q. Ou, J. Qin, M. Liu, Z. Pan, Z. Hou, TRIM25 regulates oxaliplatin resistance in colorectal cancer by promoting EZH2 stability. *Cell Death Dis.* **12**, 463 (2021).
70. L. A. Walsh, M. J. Alvarez, E. Y. Sabio, M. Reyngold, V. Makarov, S. Mukherjee, K. W. Lee, A. Desrichard, S. Turcan, M. G. Dalin, V. K. Rajasekhar, S. Chen, L. T. Vahdat, A. Califano, T. A. Chan, An integrated systems biology approach identifies TRIM25 as a key determinant of breast cancer metastasis. *Cell Rep.* **20**, 1623–1640 (2017).
71. Z. Wang, D. Tong, C. Han, Z. Zhao, X. Wang, T. Jiang, Q. Li, S. Liu, L. Chen, Y. Chen, A. Li, C. Huang, Blockade of miR-3614 maturation by IGF2BP3 increases TRIM25 expression and promotes breast cancer cell proliferation. *EBioMedicine* **41**, 357–369 (2019).
72. K. I. Takayama, T. Suzuki, T. Tanaka, T. Fujimura, S. Takahashi, T. Urano, K. Ikeda, S. Inoue, TRIM25 enhances cell growth and cell survival by modulating p53 signals via interaction with G3BP2 in prostate cancer. *Oncogene* **37**, 2165–2180 (2018).
73. Z. Zhu, Y. Wang, C. Zhang, S. Yu, Q. Zhu, K. Hou, B. Yan, RETRACTED ARTICLE: TRIM25 blockade by RNA interference inhibited migration and invasion of gastric cancer cells through TGF-β signaling. *Sci. Rep.* **6**, 19070 (2016).
74. B. A. Carneiro, W. S. El-Deiry, Targeting apoptosis in cancer therapy. *Nat. Rev. Clin. Oncol.* **17**, 395–417 (2020).
75. D. Hanahan, R. A. Weinberg, Hallmarks of cancer: The next generation. *Cell* **144**, 646–674 (2011).
76. J. P. Friedmann Angeli, M. Schneider, B. Proneth, Y. Y. Tyurina, V. A. Tyurin, V. J. Hammond, N. Herbach, M. Aichler, A. Walch, E. Eggenhofer, D. Basavarajappa, O. Radmark, S. Kobayashi, T. Seibt, H. Beck, F. Neff, I. Esposito, R. Wanke, H. Forster, O. Yefremova, M. Heinrichmeyer, G. W. Bornkamm, E. K. Geissler, S. B. Thomas, B. R. Stockwell, V. B. O'Donnell, V. E. Kagan, J. A. Schick, M. Conrad, Inactivation of the ferroptosis regulator Gpx4 triggers acute renal failure in mice. *Nat. Cell Biol.* **16**, 1180–1191 (2014).
77. B. A. Carlson, R. Tobe, E. Yefremova, P. A. Tsuji, V. J. Hoffmann, U. Schweizer, V. N. Gladyshev, D. L. Hatfield, M. Conrad, Glutathione peroxidase 4 and vitamin E cooperatively prevent hepatocellular degeneration. *Redox Biol.* **9**, 22–31 (2016).
78. A. D. Waldman, J. M. Fritz, M. J. Lenardo, A guide to cancer immunotherapy: From T cell basic science to clinical practice. *Nat. Rev. Immunol.* **20**, 651–668 (2020).
79. L. Galluzzi, I. Vitale, S. Warren, S. Adjemian, P. Agostinis, A. B. Martinez, T. A. Chan, G. Coukos, S. Demaria, E. Deutsch, D. Draganov, R. L. Edelson, S. C. Formenti, J. Fucikova, L. Gabriele, U. S. Gaipl, S. R. Gameiro, A. D. Garg, E. Golden, J. Han, K. J. Harrington, A. Hemminki, J. W. Hodge, D. M. S. Hossain, T. Illidge, M. Karin, H. L. Kaufman, O. Kepp, G. Kroemer, J. J. Lasarte, S. Loi, M. T. Lotze, G. Manic, T. Merghoub, A. A. Melcher, K. L. Mossman, F. Prosper, O. Rekdal, M. Rescigno, C. Riganti, A. Sistigu, M. J. Smyth, R. Spisek, J. Stagg, B. E. Strauss, D. Tang, K. Tatsuno, S. W. van Gool, P. Vandenabeele, T. Yamazaki, D. Zamarin, L. Zitvogel, A. Cesano, F. M. Marincola, Consensus guidelines for the definition, detection and interpretation of immunogenic cell death. *J. Immunother. Cancer* **8**, e000337 (2020).
80. G. Kroemer, C. Galassi, L. Zitvogel, L. Galluzzi, Immunogenic cell stress and death. *Nat. Immunol.* **23**, 487–500 (2022).
81. D. Tang, R. Kang, H. J. Zeh, M. T. Lotze, The multifunctional protein HMGB1: 50 years of discovery. *Nat Rev Immunol.* 2023). doi: 10.1038/s41577-023-00894-6.. Online ahead of print..
82. C. Li, Y. Zhang, X. Cheng, H. Yuan, S. Zhu, J. Liu, Q. Wen, Y. Xie, J. Liu, G. Kroemer, D. J. Klionsky, M. T. Lotze, H. J. Zeh, R. Kang, D. Tang, PINK1 and PARK2 suppress pancreatic tumorigenesis through control of mitochondrial iron-mediated immunometabolism. *Dev. Cell* **46**, 441–455.e8 (2018).
83. H. Kazama, J. E. Ricci, J. M. Herndon, G. Hoppe, D. R. Green, T. A. Ferguson, Induction of immunological tolerance by apoptotic cells requires caspase-dependent oxidation of high-mobility group box-1 protein. *Immunity* **29**, 21–32 (2008).

84. R. W. Jenkins, D. A. Barbie, K. T. Flaherty, Mechanisms of resistance to immune checkpoint inhibitors. *Br. J. Cancer* **118**, 9–16 (2018).
85. D. R. Littman, Releasing the brakes on cancer immunotherapy. *Cell* **162**, 1186–1190 (2015).
86. M. Yang, C. Li, S. Zhu, L. Cao, G. Kroemer, H. Zeh, D. Tang, R. Kang, TFAM is a novel mediator of immunogenic cancer cell death. *Onco. Targets. Ther.* **7**, e1431086 (2018).
87. S. Qin, H. Wang, R. Yuan, H. Li, M. Ochani, K. Ochani, M. Rosas-Ballina, C. J. Czura, J. M. Huston, E. Miller, X. Lin, B. Sherry, A. Kumar, G. Larosa, W. Newman, K. J. Tracey, H. Yang, Role of HMGB1 in apoptosis-mediated sepsis lethality. *J. Exp. Med.* **203**, 1637–1642 (2006).
88. A. Tesniere, F. Schlemmer, V. Boige, O. Kepp, I. Martins, F. Ghiringhelli, L. Aymeric, M. Michaud, L. Apetoh, L. Barault, J. Mendiboure, J. P. Pignon, V. Jooste, P. van Endert, M. Ducreux, L. Zitvogel, F. Piard, G. Kroemer, Immunogenic death of colon cancer cells treated with oxaliplatin. *Oncogene* **29**, 482–491 (2010).
89. J. Li, J. Liu, Y. Xu, R. Wu, X. Chen, X. Song, H. Zeh, R. Kang, D. J. Klionsky, X. Wang, D. Tang, Tumor heterogeneity in autophagy-dependent ferroptosis. *Autophagy* **17**, 3361–3374 (2021).
90. W. S. Yang, K. J. Kim, M. M. Gaschler, M. Patel, M. S. Shchepinov, B. R. Stockwell, Peroxidation of polyunsaturated fatty acids by lipoxygenases drives ferroptosis. *Proc. Natl. Acad. Sci. U.S. A.* **113**, E4966–E4975 (2016).
91. W. Zou, D.-E. Zhang, The interferon-inducible ubiquitin-protein isopeptide ligase (E3) EFP also functions as an ISG15 E3 ligase. *J. Biol. Chem.* **281**, 3989–3994 (2006).
92. J. Elegheert, E. Behiels, B. Bishop, S. Scott, R. E. Woolley, S. C. Griffiths, E. F. X. Byrne, V. T. Chang, D. I. Stuart, E. Y. Jones, C. Siebold, A. R. Aricescu, Lentiviral transduction of mammalian cells for fast, scalable and high-level production of soluble and membrane proteins. *Nat. Protoc.* **13**, 2991–3017 (2018).
93. F. A. Ran, P. D. Hsu, J. Wright, V. Agarwala, D. A. Scott, F. Zhang, Genome engineering using the CRISPR-Cas9 system. *Nat. Protoc.* **8**, 2281–2308 (2013).
94. M. Kornete, R. Marone, L. T. Jeker, Highly efficient and versatile plasmid-based gene editing in primary T cells. *J. Immunol.* **200**, 2489–2501 (2018).

Acknowledgments: We thank D. Primm (Department of Surgery, University of Texas Southwestern Medical Center) for critical reading of the manuscript. **Funding**: Research by D.T. and R.K. was supported by grants from the National Institutes of Health (R01CA160417, R01CA229275, and R01CA211070). **Author contributions:** J. Li, J. Liu, Z.Z., X.C., R.W., C.Y., R.K., and D.T. carried out the simulations and sample preparation and analyzed the data. J. Li, D.T., and R.K. wrote the paper. B.S. provided key reagents. G.K. and B.S. assisted in data interpretation and edited the manuscript. **Competing interests:** The authors declare that they have no competing interests. **Data and materials availability:** All data associated with this study are present in the paper or the Supplementary Materials. Materials (TRIM25 plasmids and GPX4 plasmids) generated in this study are available for noncommercial research purposes under a material transfer agreement by contacting the corresponding author.

Submitted 14 December 2022
Resubmitted 07 July 2023
Accepted 26 September 2023
Published 1 November 2023
10.1126/scitranslmed.adg3049

Science Translational Medicine

Tumor-specific GPX4 degradation enhances ferroptosis-initiated antitumor immune response in mouse models of pancreatic cancer

Jingbo Li, Jiao Liu, Zhuan Zhou, Runliu Wu, Xin Chen, Chunhua Yu, Brent Stockwell, Guido Kroemer, Rui Kang, and Daolin Tang

Sci. Transl. Med. **15** (720), eadg3049. DOI: 10.1126/scitranslmed.adg3049

Science Translational Medicine (ISSN 1946-6242) is published by the American Association for the Advancement of Science. 1200 New York Avenue NW, Washington, DC 20005. The title *Science Translational Medicine* is a registered trademark of AAAS.

Science Translational Medicine
AAAS

Supplementary Materials for

Tumor-specific GPX4 degradation enhances ferroptosis-initiated antitumor immune response in mouse models of pancreatic cancer

Jingbo Li *et al.*

Corresponding author: Daolin Tang, daolin.tang@utsouthwestern.edu; Rui Kang, rui.kang@utsouthwestern.edu

Sci. Transl. Med. **15**, eadg3049 (2023)
DOI: 10.1126/scitranslmed.adg3049

The PDF file includes:

Other Supplementary Material for this manuscript includes the following:

Supplementary Materials

Materials and Methods

Cell growth assay

Cells were seeded at 1×10^4 cells per well into 96-well plates and incubated with indicated drugs in triple wells. Subsequently, 100 μl of fresh medium was added to cells containing 10 μl of Cell Counting Kit-8 solutions (Bimake, B34304) and incubated for 1 hour (5% CO_2 at 37 ℃). Absorbance at 450 nm was measured using a microplate reader (BioTek Cytation 5). A colony formation assay was designed to evaluate the proliferative ability of cells in the long-term. Briefly, cells were pretreated with DMSO or N6F11 for 12 hours. A total of 500 cancer cells were plated in a 6-well plate and were allowed to form colonies for 10 days, which were visible after being stained with 0.5% crystal violet (Sigma-Aldrich, C0775) for 10 minutes.

Cell death assay

Cells were seeded at a density of 2×10^5 cells/well in 6-well plates. The next day, cells were incubated with the indicated treatments. After that, the cells were stained with propidium iodide (Thermo Fisher Scientific, R37108) for 15-30 minutes in an incubator of 5% CO_2 at 37 °C. Morphological changes were examined by fluorescence microscope at ×20 magnification. A Countess II FL Automated Cell Counter (Thermo Fisher Scientific) was used to assay the percentages of dead cells after propidium iodide staining. Furthermore, N6F11-induced cell death was confirmed using flow cytometry assays with Annexin V/propidium iodide staining.

Cycloheximide chase assay

The protein degradation rate of GPX4 was tested in the indicated PANC1 and HT1080 cells after treatment with N6F11 in the absence or presence of CHX (10 μM) for indicated times. Whole-cell lysates were analyzed for GPX4 and ACTB by western blot analyses. Band densities were normalized to the untreated group at the 0 time point, which was set at 1 arbitrary unit (AU).

Lipid peroxidation assay

Cells were seeded at 1×10^5 cells per well into 12-well plates and incubated with the indicated treatments in 5% CO_2 at 37 °C. During the last 30 minutes of incubation, 0.1 μg/ml of Hoechst 33342 (Thermo Fisher Scientific, 62249) and 10 μM BODIPY 581/591 C11 (Thermo Fisher Scientific, D3861) dyes were added. After the cells were washed with PBS, they were imaged using an EVOS imaging system (Thermo Fisher Scientific). Image analysis was conducted with ImageJ software based on 5 random fields. The relative lipid ROS was quantified by using the ratio of green fluorescence intensity (BODIPY 581/591 C11-oxidized) to red fluorescence intensity (BODIPY 581/591 C11-reduced) (*90*).

In addition, a Click-iT linoleamide alkyne (LAA) kit (Thermo Fisher Scientific, C10446) was used to detect lipid peroxidation in cells. In brief, cells were incubated with 50 μM of LAA for 1-2 hours at 37 °C, then fixed with 4% formaldehyde for 15 minutes at room temperature. Next, the cells were washed 3 times with PBS, permeabilized with 0.05% Triton X-100 for 10 minutes, and blocked with 1% bovine serum albumin (BSA) for 30 minutes. Then the cells were washed, and the click reaction was performed with 5 μM Alexa Fluor 488 azide for 30 minutes. Finally, the cells were washed 1 time with 1% BSA and 2 times with PBS, and then imaged on an EVOS Cell Imaging System (Thermo Fisher Scientific). The signal intensity was quantified using ImageJ software (n = 5 random fields).

Western blot analysis

Cells were washed by cold 4 °C phosphate-buffered saline (PBS; Sigma-Aldrich, P5493) buffer and then lysed in Cell Lysis Buffer (Cell Signaling Technology, 9803) with a protease and phosphatase inhibitor single-use cocktail (Thermo Fisher Scientific, 78442) for 30 minutes on ice. Proteins were quantified by using a bicinchoninic acid (BCA) assay (Thermo Fisher Scientific, 23225), and 20-25 μg of each sample was resolved on 4%-12% Criterion XT Bis-Tris gels (Bio-Rad, 3450124) in XT MES running buffer (Bio-Rad, 1610789) and transferred to polyvinylidene fluoride membranes (Bio-Rad, 1620233) with the Trans-Blot Turbo transfer system (Bio-Rad).

The membranes were incubated in 5% skim milk (Cell Signaling Technology, 9999) for 1 hour at room temperature and then incubated with indicated primary antibodies (1:500-1:1000) diluted in 5% BSA at 4 ℃ overnight. After 3 washes with PBST, membranes were incubated with goat anti-mouse or goat anti-rabbit immunoglobulin G (IgG) horseradish peroxidase secondary antibodies (1:5000; Cell Signaling Technology, 7074 and 7076) at room temperature for 1 hour and washed 3 times. SuperSignal West Pico Chemiluminescent Substrate (Thermo Fisher Scientific, 34080) or Super Signal West Femto Maximum Sensitivity Substrate (Thermo Fisher Scientific, 34095) were applied, and blots were analyzed using the ChemiDoc Touch Imaging System (Bio-Rad) and Image Lab Software (Bio-Rad). The relative intensities of the bands were automatically analyzed and normalized to a loading control. The information on antibodies is shown in **Table S1**.

qPCR assay

Total RNA was prepared by using an E.Z.N.A. HP Total RNA Kit (Omega Bio-Tek, R6812) following the manufacturer's instructions. First-strand cDNA was synthesized from 1 μg of RNA using the iScript cDNA Synthesis Kit (Bio-Rad, 1708890). Briefly, 20-μl reactions were prepared by combining 4 μl of iScript Select reaction mix, 2 μl of gene-specific enhancer solution, 1 μl of reverse transcriptase, 1 μl of gene-specific assay pool (20×, 2 μM), and 12 μl of RNA diluted in ribonuclease-free water. The cDNA from various cell samples was then amplified by real-time qPCR with specific primers using the CFX96 Touch Real-Time PCR Detection System (Bio-Rad) with CFX Manager Software (Bio-Rad). The gene expression was calculated by the $2^{-\Delta\Delta Ct}$ method and normalized to *18SRNA*. The relative concentrations of mRNA were expressed in arbitrary units based on the untreated group, which was assigned a value of 1. The primers, which were synthesized and desalted from Sigma-Aldrich, are shown in **Table S2**.

Preparation of DNA constructs

GFP-GPX4 plasmids were a gift from Brent R. Stockwell (*91*). A series of GPX4

point mutants: K48R, K125R, K127R, K135R, and K151R, were generated from the wild-type GFP-GPX4 construct by a NEB Q5 Site-Directed Mutagenesis Kit (New England BioLabs, E0554S) and the designed primers (**Table S2**). Briefly, PCR amplification by the kit's Q5 Hot Start High-Fidelity DNA Polymerase was performed with the designed primers using the wild-type plasmids as templates to generate linear plasmids. The amplified material was added directly to a unique T4 Polynucleotide Kinase and T4 Ligase-DpnI (KLD) enzyme mix for rapid (5 minutes) room temperature circularization and template removal, and finally used for the transformation of NEB 5-alpha with standard techniques. FLAG-TRIM25 was a gift from Dong-Er Zhang (*92*). The series of TRIM25 domain mutants, namely the RING domain (F-TRIM25-RING, deletion of 223-630 AA), CC domain (F-TRIM25-CC, deletion of 1-54 AA and 438-630 AA), PS domain (F-TRIM25-PS, deletion of 1-307 AA), and deletion of the PS domain (F-TRIM25-ΔPS, deletion of 307-630 AA) were generated from the wild-type FLAG-TRIM25 construct by the NEB Q5 Site-Directed Mutagenesis Kit with designed primers (**Table S2**). Sequencing verified the presence of point mutations or deletions in the plasmid.

RNA interference, gene transfection, and gene editing

The transfection of shRNA, siRNA, or cDNA was performed with Lipofectamine 3000 (Thermo Fisher Scientific, L3000-015) according to the manufacturer's protocol. For the transfection of shRNA, 293FT cells (Thermo Fisher Scientific, R70007) were used to produce high-titer lentiviral particles, and the virus-containing medium was harvested 48 hours after transfection. RNAi was performed using lentiviral transduction as previously described (*93*). Puromycin (5 μg/ml; InvivoGen, ant-pr-1) was used for the selection of transduced cells. CRISPR-Cas9–mediated gene editing was performed in close adherence to Feng Zhang lab's protocol (*94*). Neon Transfection System (Thermo Fisher Scientific) was used to transfect TRIM25 cDNA in $CD8^+$ T cells as previously described (*95*). The sequence or order information of shRNA, siRNA, gRNA, and cDNA are shown in **Table S2**.

IP and Co-IP analysis

Cells were lysed at 4 °C in ice-cold IP buffer (2% sodium dodecyl sulfate [SDS], 10 mM Tris-HCl [pH8.0], 150 mM NaCl+protease inhibitor cocktail) or Co-IP buffer (10 mM Tris-HCl [pH8.0], 150 mM NaCl, 1 mM EDTA, 0.5% NP40+protease inhibitor cocktail), and cell lysates were cleared by brief centrifugation (13,000*g*, 15 minutes). Concentrations of proteins in the supernatant were determined using the BCA assay (Thermo Fisher Scientific, 23225). Before immunoprecipitation, samples containing equal amounts of proteins were precleared with protein A agarose beads (4 °C, 3 hours; Santa Cruz Biotechnology, sc-2027) and subsequently incubated with various irrelevant IgG or specific antibodies (3-5 μg/ml) in the presence of protein A agarose beads for 2 hours or overnight at 4 °C with gentle shaking. Following incubation, agarose beads were washed extensively with PBS, and proteins were eluted by boiling in 2× SDS sample buffer before SDS–polyacrylamide gel electrophoresis.

Tandem mass spectrometry

Proteolytic peptides from in-gel trypsin digestion were analyzed using nanoflow reverse-phased liquid chromatography tandem mass spectrometry (LC-MS/MS). Tryptic peptides were loaded onto a C18 column (PicoChip column packed with 10.5-cm ReproSil C18 [3 μm and 120 Å] chromatography media with the column having an internal diameter of 75 μm and a tip of 15 μm; New Objective, Inc.). Loading was performed using a Dionex HPLC system (Thermo Fisher Scientific, Dionex UltiMate 3000) operated with a double-split system to provide an in-column nanoflow rate (~300 nl/minute). Mobile phases used were 0.1% formic acid for A and 0.1% formic acid in ACN for B. Peptides were eluted off the column using a 52-minute gradient (2% to 40% B for 42 minutes, 40% to 95% B for 1 minute, 95% B for 1 minute, and 2% B for 8 minutes) and injected into a linear ion trap MS (Thermo Fisher Scientific, LTQ XL) through electrospray.

The LTQ XL was operated in a date-dependent MS/MS mode in which each full MS spectrum (acquired at 30,000 automatic gain control [AGC] targets, 50-ms maximum ion accumulation time, and a precursor ion selection range with a

mass/charge ratio of 375 to 1800) was followed by MS/MS scans of the eight most abundant molecular ions determined from a full MS scan (acquired on the basis of the setting of 1000 signal thresholds, 10,000 AGC targets, 100-ms maximum accumulation time, 2.0-Da isolation width, 30-ms activation time, and 35% normalized collision energy). Dynamic exclusion was enabled to minimize the redundant selection of peptides previously selected for collision-induced dissociation.

Peptide identification by database search

MS/MS spectra were searched using the Mascot search engine (version 2.4.0, Matrix Science Ltd.) against the UniProt human proteome database. The modifications used were the following: static modification of cysteine (carboxyamidomethylation, +57.05 Da), variable modification of methionine (oxidation, +15.99 Da), and protein N-terminal acetylation. The mass tolerance was set to 1.4 Da for the precursor ions and 0.8 Da for the fragment ions. Peptide identifications were filtered using PeptideProphet and ProteinProphet algorithms with a protein threshold cutoff of 99% and a peptide threshold cutoff of 90% implemented in Scaffold (Proteome Software).

Biochemical assay

The concentrations or activity of HMGB1 (Shino-Test Corporation, ST51011), GSH (Abcam, ab239727), GPX (Abcam, ab102530), GPX4 (LSBio, LS-F53129-1), MDA (Sigma-Aldrich, MAK085), IFNG (R&D Systems, MIF00), IL2 (R&D Systems, M2000) or selenium (abbexa, abx298910) in indicated samples were measured using ELISA according to the manufacturer's guidelines. Measurement of alkaline phosphatase (ALT) and blood urea nitrogen (BUN) in the serum was performed using an IDEXX Catalyst Dx Chemistry Analyzer.

CETSA

For intact-cell CETSA experiments, cells were treated with indicated compounds or DMSO for 1 hour at 37 °C. Cells were collected, washed with PBS (pH 7.4), and centrifuged at 500*g* for 5 minutes. Cells were resuspended in PBS (pH 7.4) and

aliquoted into PCR tubes (50 µl volume, ~1 million cells per condition) for heating at different temperatures (43-64 °C in 3 °C increments) in a thermocycler for 3 minutes. Samples were allowed to cool to room temperature for an additional 3 minutes. Cells were lysed by three freeze-thaw cycles in liquid nitrogen and subsequent incubation on ice with occasional vortexing for 20 minutes. After lysis, lysates were centrifuged at 20,000*g* (4 °C) for 10 minutes to remove insoluble material. The soluble fraction was diluted with 6× SDS loading buffer for western blotting analysis.

Purification of full-length TRIM25

293T cells were transfected with FLAG-TRIM25 (Addgene, 12449) plasmid and grown for 72 h. Cells were washed with cold PBS and lysed in NP40 lysis buffer (50 mM Tris [pH 8.0], 1% NP40, 150 mM NaCl, 10% glycerol, 1 mM tris (2-carboxyethyl) phosphine [TCEP], and 25 U/mL of benzonase) containing proteinase inhibitor cocktail (Roche). Cells were lysed and sonicated (Branson Digital Sonifier, set to 50% amplitude) three times for two seconds each, with a one-minute rest on ice between each two-second pulse, and then kept on ice for 30 minutes with vortex occasionally. Lysates were centrifuged at 20,000 g for 20 minutes at 4°C to pellet cell debris. Clarified cell lysates were purified FLAG immunoprecipitation kit (Sigma). The FLAG-TRIM25 protein was eluted with 3× FLAG peptides according to the manufacturer's protocol. Purified proteins were flash-frozen with liquid nitrogen and stored at -80°C.

Ubiquitination assays

TRIM25 proteins (200 nM) were incubated at 37 °C with E1 (100 nM), E2 (1 µM UbcH5b), 200 nM His-GPX4, N6F11 (0.1 µM or 1 µM) and ubiquitin (40 µM) in reaction buffer (50 mM Tris [pH 7.5], 150 mM NaCl, 0.5 mM TCEP, 5 mM ATP, and 10 mM $MgCl_2$). Reactions were stopped by the addition of SDS-PAGE sample buffer and boiling for 10 min. Expression of Ub, HA and His tags were analyzed using western blot. For Ni^{2+}-agarose pull-down, the reaction was diluted 1:1 (v/v) in equilibration buffer (50 mM Tris [pH 7.5], 300 mM NaCl, and 10 mM imidazole), then 20 µl of Ni-NTA resin was added and allowed to react for 1 hour at 4 °C. The resin was pelleted at

700 × g and washed 3 times with wash buffer (50 mM Tris [pH 7.5], 300 mM NaCl, and 25 mM imidazole). Finally, the Ni^{2+}-agarose pull-down solution was eluted with SDS-PAGE sample buffer and boiled for 10 min.

Immunohistochemistry analysis

Formalin-fixed, paraffin-embedded tumor tissue sections (5 μm thick) were tested using antibodies against CD8α (1:200; Cell Signaling Technology, 98941) according to standard procedures. Briefly, slides were deparaffinized in xylene and rehydrated with decreasing concentrations of ethanol in water. Antigen retrieval was performed by preheating sodium citrate buffer (pH 6.0) in a microwave oven for 2 minutes, then incubating slides at sub-boiling temperature (95-98 C°) for 10 minutes and cooling at room temperature for 30 minutes. Endogenous peroxidases were quenched by incubating slides in 3% hydrogen peroxide for 10 minutes. Sections were then washed twice with PBS for 5 minutes each. Endogenous avidin and biotin were blocked using 1× Animal-Free Blocking Solution (Cell Signaling Technology, 15019). Sections were then washed twice with PBS for 5 minutes each. Primary antibodies were applied overnight in a humidified chamber at 4 °C. After rinsing slides in PBS, they were incubated in 1-3 drops of SignalStain Boost IHC Detection Reagent (HRP, Rabbit; Cell Signaling Technology, 8114) for 30 minutes at room temperature. After washing 3 times with PBS for 5 minutes each, slides were incubated with SignalStain DAB (Cell Signaling Technology, 8059) for 2-5 minutes, depending on the primary antibody. After washing in distilled water, sections were counterstained with hematoxylin (Cell Signaling Technology, 14166), dehydrated by ethanol and xylene, and coverslipped using SignalStain Mounting Medium (Cell Signaling Technology, 14177). Images were collected and quantified based on 5-8 fields using an EVOS microscope (Invitrogen).

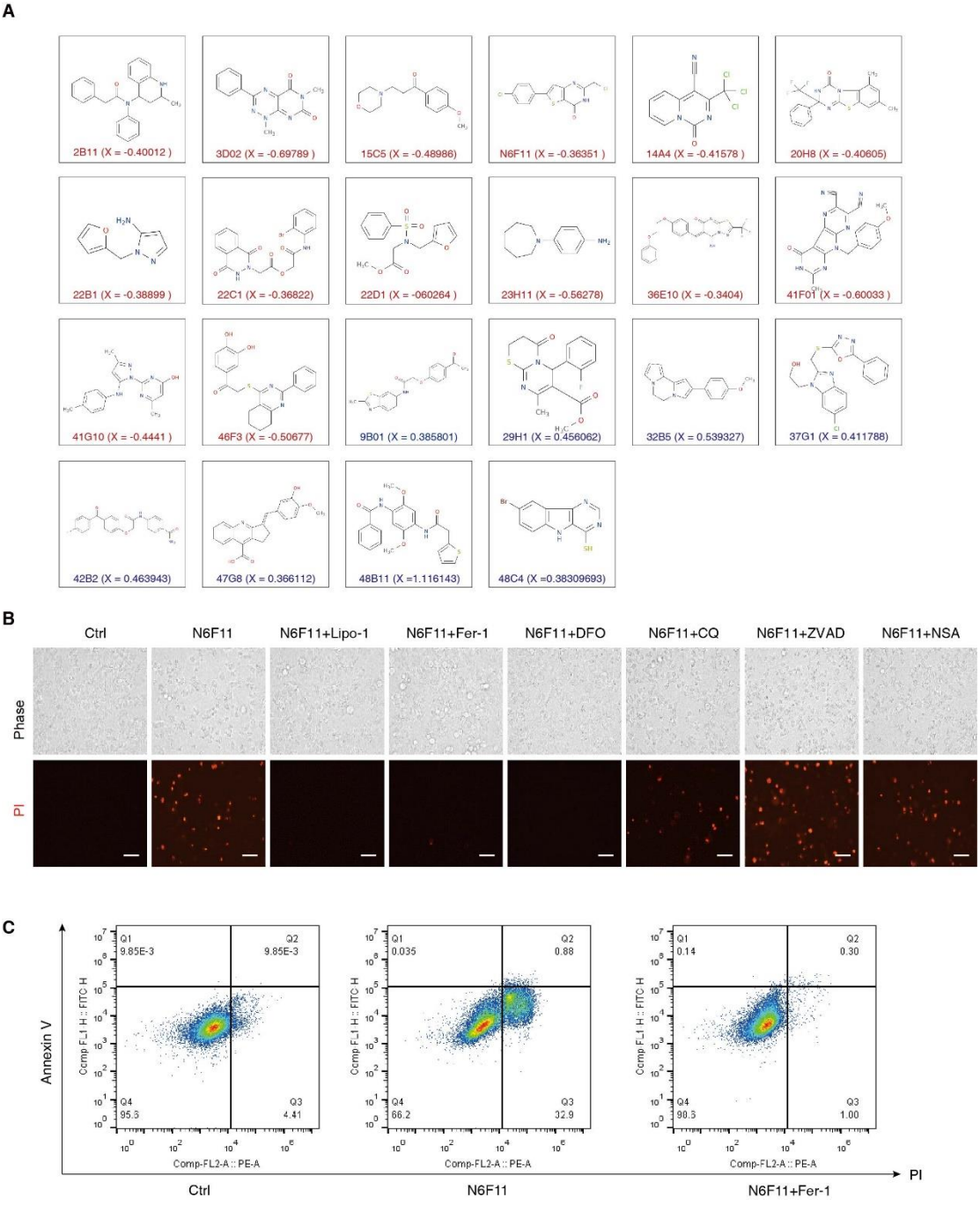

Fig. S1. Identification of N6F11 as a GPX4 degrader and inducer of ferroptosis. **(A)** Structures of compounds that inhibit (red) or increase (blue) GPX4 expression in PANC1 cells. **(B)** PI staining for cell death analysis of PANC1 cells following treatment with N6F11 (5 μM) in the absence or presence of liproxstatin-1 (Lipo-1; 1 μM), ferrostatin-1 (Fer-1; 1 μM), deferoxamine (DFO; 100 μM), Z-VAD-FMK (ZVAD; 20 μM), necrosulfonamide (NSA; 1 μM), or chloroquine (CQ; 50 μM) for 12 hours (bar =

50 μm). **(C)** Flow cytometry assays using Annexin V/PI staining confirmed that N6F11 (5 μM)-induced PI-positive cells were inhibited by treatment with ferrostatin-1 (1 μM).

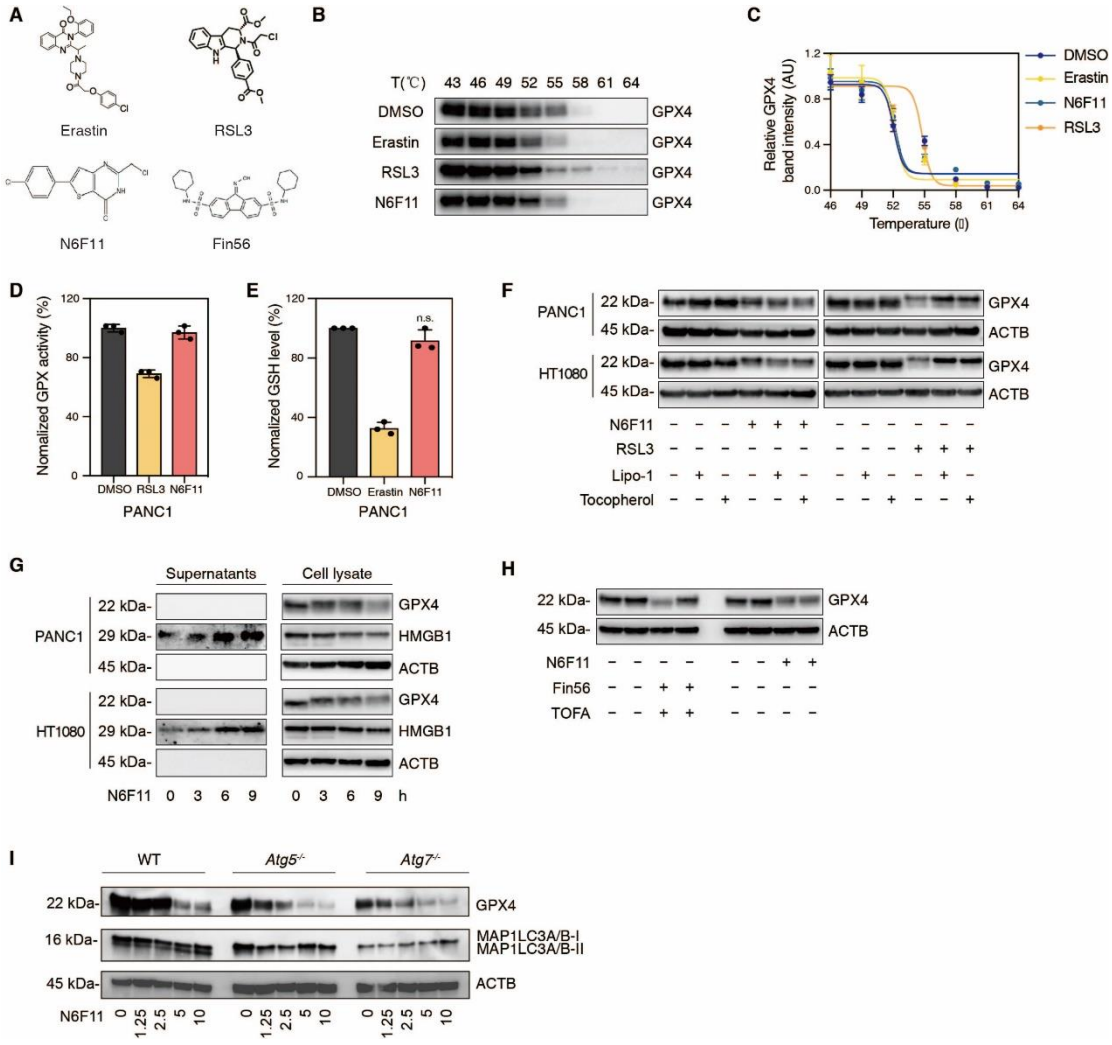

Fig. S2. N6F11 is different from other known ferroptosis activators. (A) Structures of indicated ferroptosis activators. **(B)** Effects of indicated compounds on thermal stability of GPX4 protein in PANC1 cells. **(C)** Effects of indicated compounds on thermal stability of GPX4 protein in PANC1 cells (n = 3 biologically independent samples; data are presented as mean ± SD). **(D)** Analysis of GPX activity in PANC1 cells following treatment with RSL3 (0.5 μM) or N6F11 (5 μM) for 12 hours. **(E)** Analysis of GSH concentration in PANC1 cells following treatment with erastin (5 μM) or N6F11 (5 μM) for 12 hours. **(F)** Western blot analysis of GPX4 expression in PANC1 cells following treatment with RSL3 (0.5 μM) or N6F11 (5 μM) in the absence or presence of liproxstatin-1 (Lipo-1; 1 μM) or tocopherol (100 μM) for 12 hours. **(G)** Western blot analysis of indicated proteins in supernatants or whole cell lysate of PANC1 cells following treatment with N6F11 (5 μM) for 3-9 hours. **(H)** Western blot

analysis of GPX4 expression in PANC1 cells following treatment with Fin56 (5 μM) or N6F11 (5 μM) in the absence or presence of TOFA (50 μM) for 12 hours. **(I)** Western blot analysis of protein expression in indicated MEFs following treatment with N6F11 (1.25-10 μM) for 12 hours.

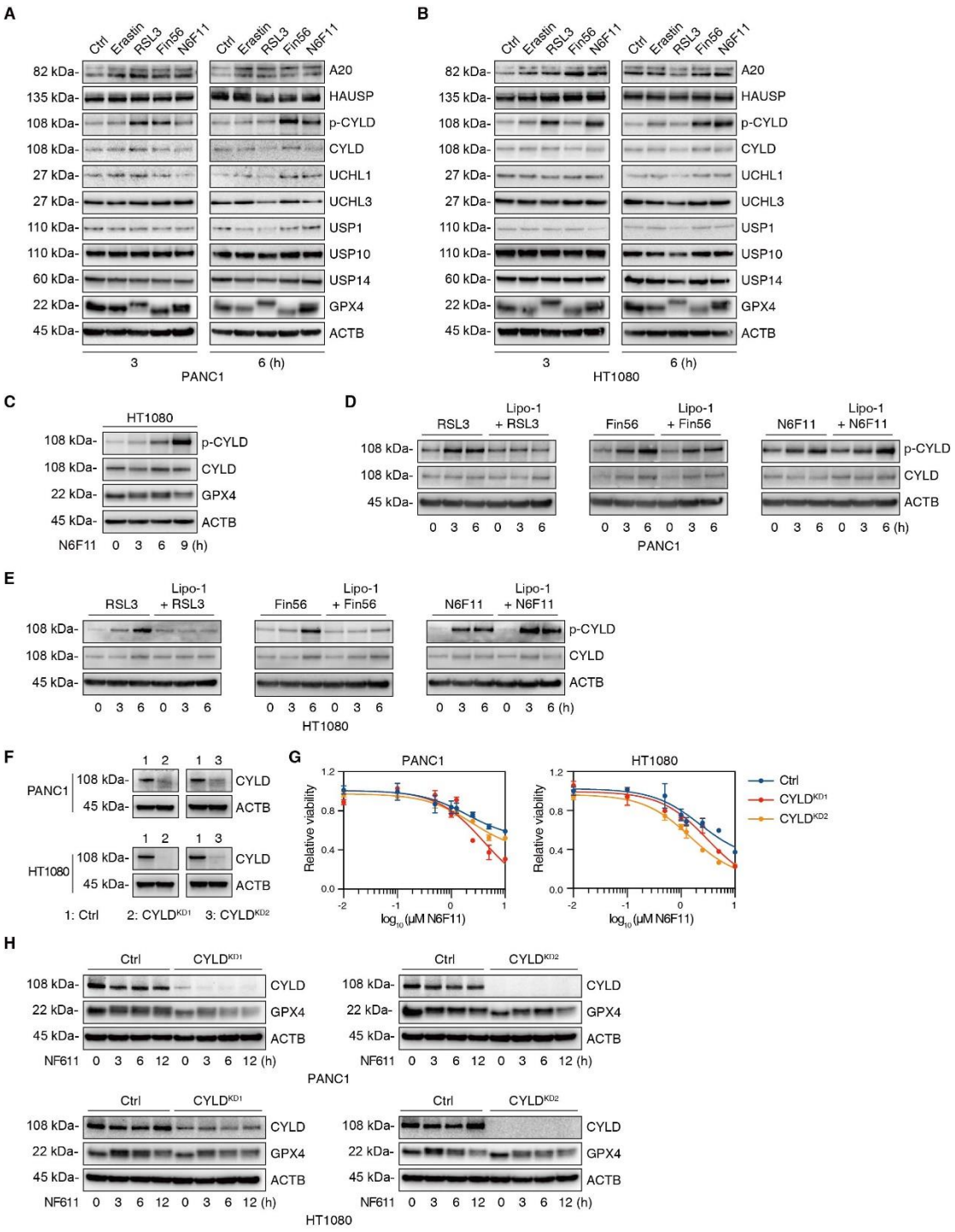

Fig. S3. CYLD is not required for N6F11-induced GPX4 degradation and ferroptosis. (A) Western blot analysis of indicated deubiquitinase family expression in PANC1 cells following treatment with erastin (5 μM), RSL3 (0.5 μM), Fin56 (5 μM) or N6F11 (5 μM) for 3-6 hours. **(B)** Western blot analysis of indicated deubiquitinase family expression in HT1080 cells following treatment with erastin (5 μM), RSL3 (0.5 μM), Fin56 (5 μM) or N6F11 (5 μM) for 3-6 hours. **(C)** Effects of N6F11 on the

phosphorylation of CYLD in HT1080 cells following treatment with N6F11 (5 μM) for 3-9 hours. **(D)** Western blot analysis of indicated protein expression in PANC1 cells following treatment with RSL3 (0.5 μM), Fin56 (5 μM), or N6F11 (5 μM) in the absence or presence of liproxstatin-1 (Lipo-1; 1 μM) for 3-6 hours. **(E)** Western blot analysis of indicated protein expression in HT1080 cells following treatment with RSL3 (0.5 μM), Fin56 (5 μM), or N6F11 (5 μM) in the absence or presence of liproxstatin-1 (Lipo-1; 1 μM) for 3-6 hours. **(F)** Western blot analysis of CYLD expression in indicated CYLD-knockdown ($CYLD^{KD}$) cells. **(G)** Cell viability of indicated wild-type and CYLD-knockdown ($CYLD^{KD}$) cells following treatment with N6F11 for 24 hours (n = 3 biologically independent samples; data are presented as mean ± SD). **(H)** Western blot analysis of GPX4 expression in indicated wild-type and CYLD-knockdown ($CYLD^{KD}$) cells following treatment with N6F11 for 3-12 hours.

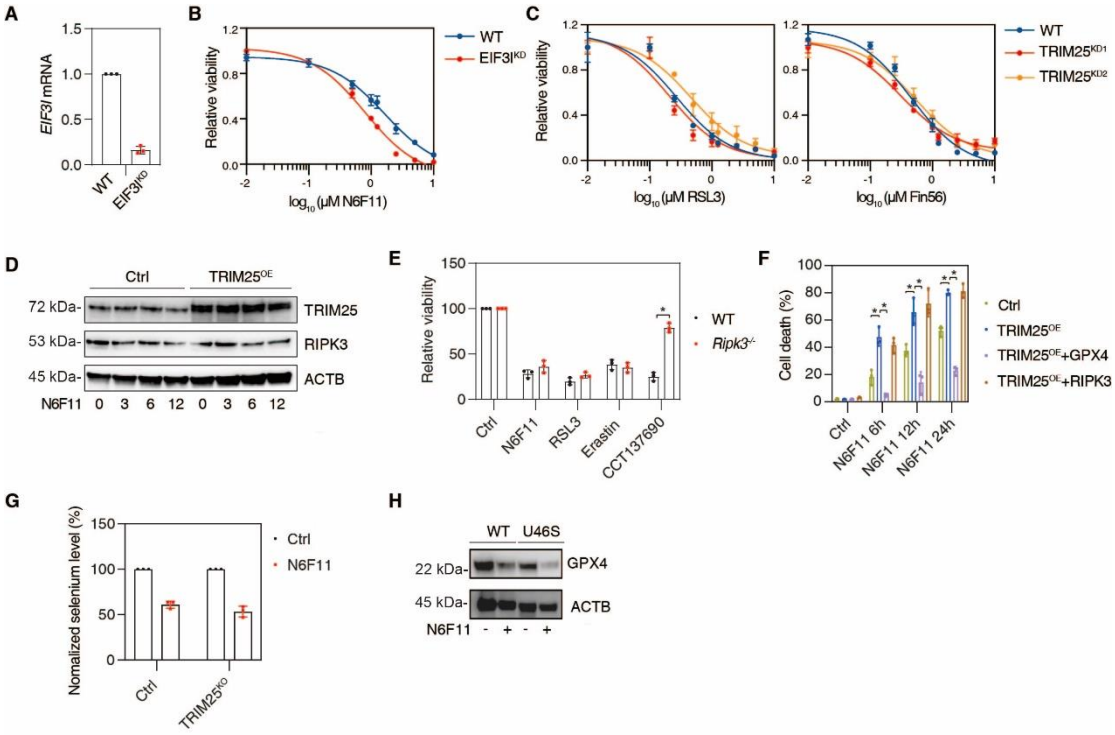

Fig. S4. EIF3I and RIPK3 are not required for N6F11-induced ferroptosis. (A) qPCR analysis of EIF3I mRNA expression in wild-type and EIF3I-knockdown ($EIF3I^{KD}$) HT1080 cells (n = 3 biologically independent samples; data are presented as mean ± SD). **(B)** Cell viability of indicated HT1080 cells following treatment with N6F11 (n = 3 biologically independent samples; data are presented as mean ± SD). **(C)** Cell viability of indicated HT1080 cells following treatment with RSL3 or Fin56 (n = 3 biologically independent samples; data are presented as mean ± SD). **(D)** Western blot analysis showing RIPK3 expression in indicated PANC1 cells following treatment with N6F11 for 3-12 hours. **(E)** Cell viability of indicated MEF cells following treatment with N6F11 (2 μM), RSL3 (0.5 μM), erastin (1 μM), or CCT137690 (5 μM) for 24 hours (n = 3 biologically independent samples; $*P < 0.05$, *t* test; data are presented as mean ± SD). **(F)** Cell death of indicated PANC1 cells following treatment with N6F11 (5 μM) for 6-24 hours (n = 3 biologically independent samples; $*P < 0.05$, two way ANOVA test; data are presented as mean ± SD). **(G)** ELISA analysis of intracellular selenium concentrations in indicated PANC1 cells following treatment with N6F11 (5 μM) for 12 hours (n = 3 biologically independent samples; data are presented as mean ± SD). **(H)** Western blot analysis showing GPX4 expression in indicated wild-type or

U46S GPX4 mutation PANC1 cells following treatment with N6F11 (10 μM) for 12 hours.

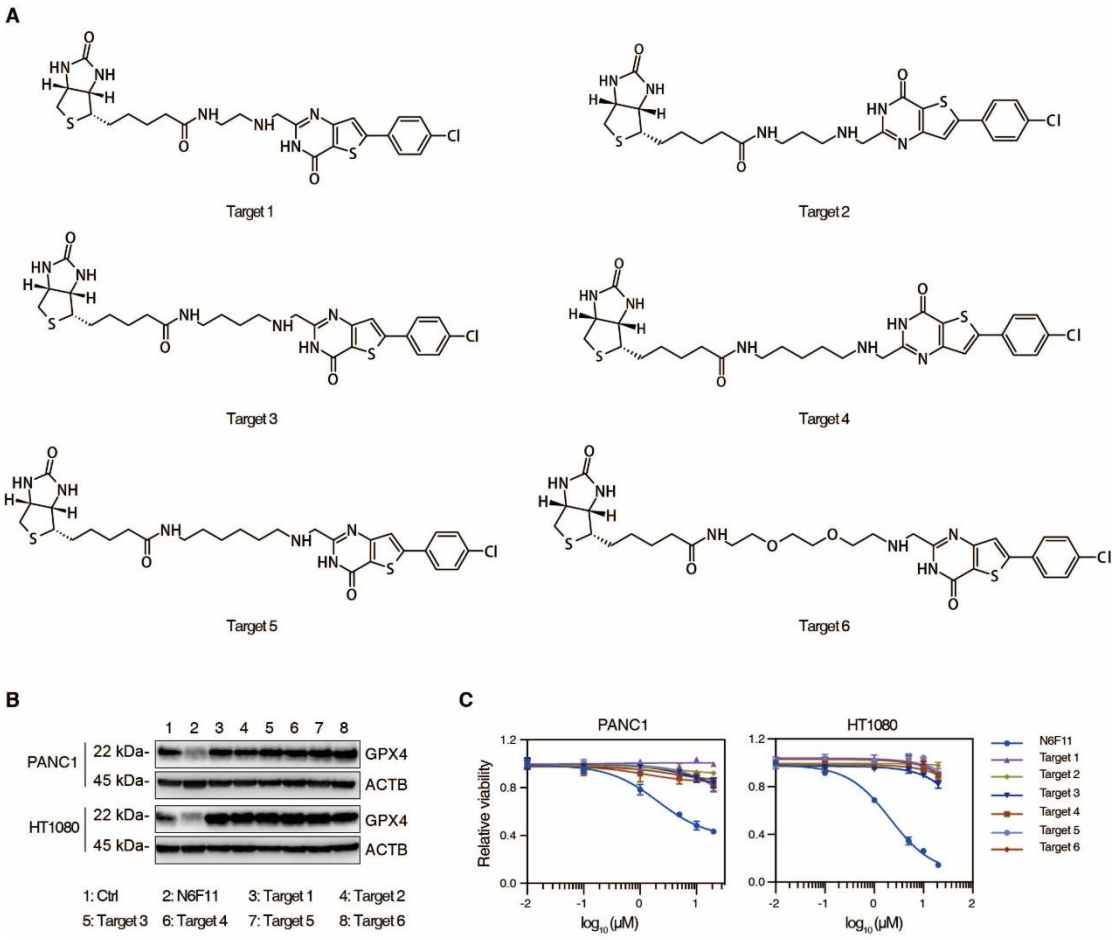

Fig. S5. The chloride group between two nitrogen atoms is essential for N6F11 activity. (A) Structure of N6F11 analogs (targets 1-6). **(B)** Western blot analysis of GPX4 expression in indicated cells following treatment with N6F11 and its analogs for 12 hours. **(C)** Analysis of cell viability in indicated cells following treatment with N6F11 and its analogs for 24 hours (n = 3 biologically independent samples; data are presented as mean ± SD).

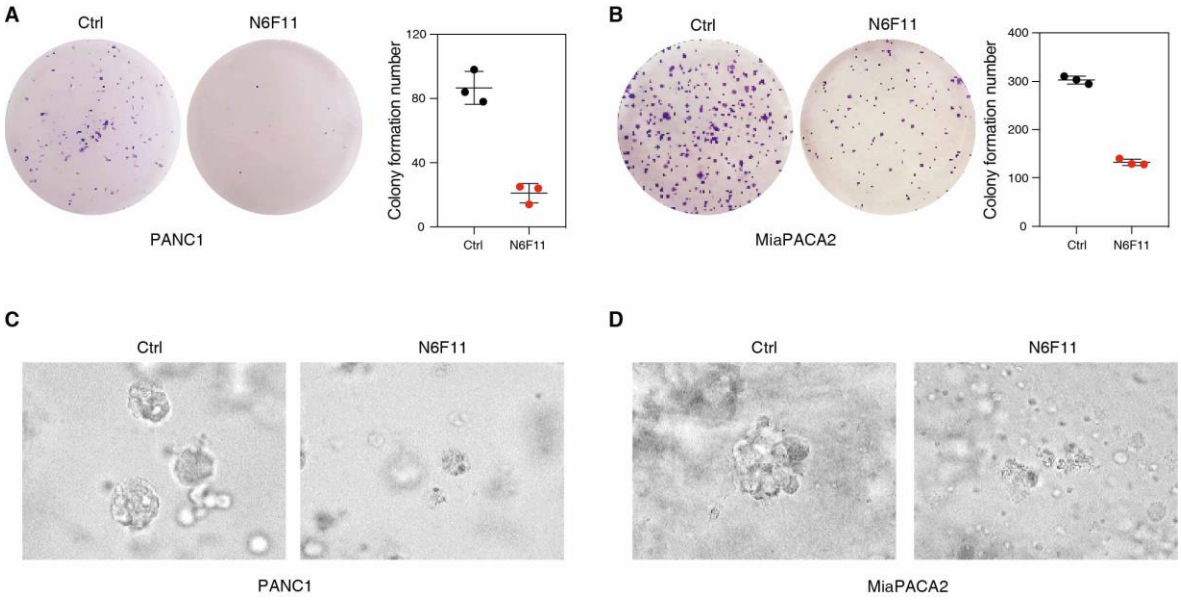

Fig. S6. N6F11 suppresses the growth of human PDAC. (A) PANC1 cells were pretreated with DMSO or N6F11 (5 μM) for 12 hours. A total of 500 cancer cells were plated in a 6-well plate and were allowed to form colonies for 10 days. Representative images and quantitative analysis of the results of the colony formation assay are shown. **(B)** MiaPACA2 cells were pretreated with DMSO or N6F11 (5 μM) for 12 hours. A total of 500 cancer cells were plated in a 6-well plate and were allowed to form colonies for 10 days. Representative images and quantitative analysis of the results of the colony formation assay are shown. **(C)** Effects of N6F11 on the growth of 3D PANC1 tumor spheroids for increasing periods of time; representative pictures of spheroids are shown. **(D)** Effects of N6F11 on the growth of 3D MiaPACA2 tumor spheroids for increasing periods of time; representative pictures of spheroids are shown.

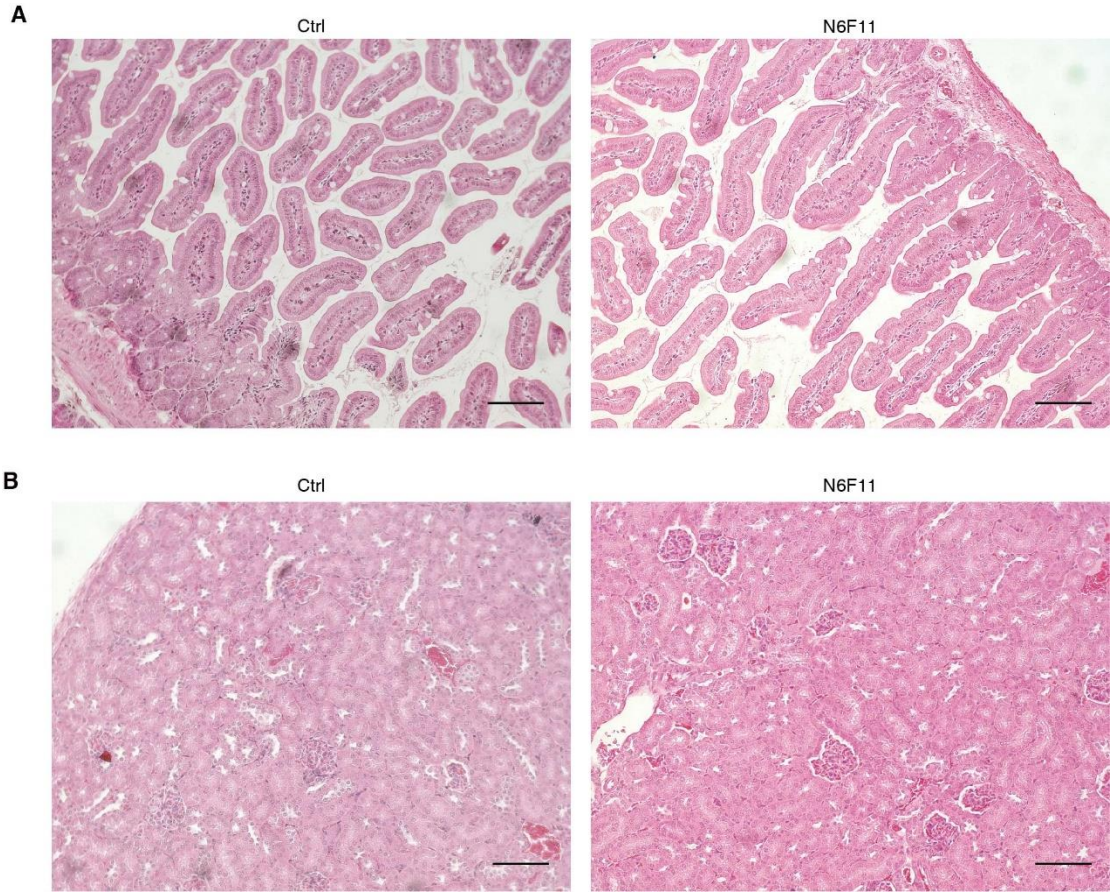

Fig. S7. Histological analysis. (A) Hematoxylin and eosin staining of intestinal tissues in C57BL/6 mice inoculated with 1×10^6 KPC tumor cells and treated with N6F11 (10 mg/kg) on day 14. Bar=200 μm. **(B)** Hematoxylin and eosin staining of kidney tissues in C57BL/6 mice inoculated with 1×10^6 KPC tumor cells and treated with N6F11 (10 mg/kg) on day 14. Bar=200 μm

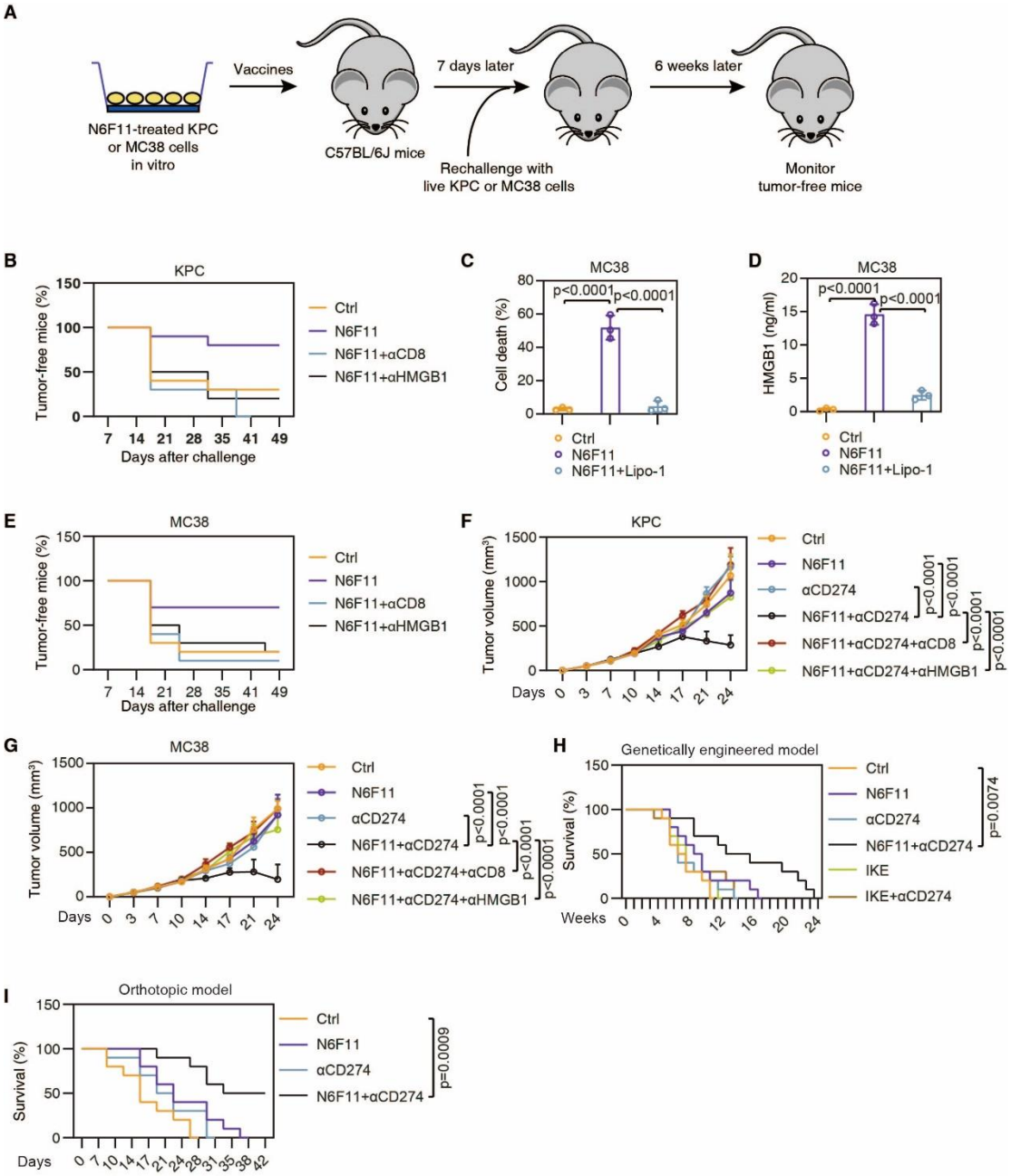

Fig. S8. Application of N6F11 in tumor immunotherapy. (A) *In vivo* prophylactic tumor vaccination model. **(B)** The capacity of N6F11-treated tumor cells to vaccinate against KPC cells in C57BL/6J mice. The percentage of tumor-free mice is indicated (n = 10 mice/group). **(C)** MC38 cells were treated with N6F11 (5 μM) in the absence or presence of liproxstatin-1 (Lipo-1; 1 μM) for 12 hours. Cell death was assayed (n = 3 biologically independent samples; $*P < 0.05$, one-way ANOVA with Tukey's multiple comparisons test; data are presented as mean ± SD). **(D)** MC38 cells were treated with

N6F11 (5 μM) in the absence or presence of liproxstatin-1 (Lipo-1; 1 μM) for 12 hours. HMGB1 release was assayed (n = 3 biologically independent samples; *$P < 0.05$, one-way ANOVA with Tukey's multiple comparisons test; data are presented as mean ± SD). **(E)** The capacity of N6F11-treated tumor cells to vaccinate against MC38 cells in C57BL/6J mice. The percentage of tumor-free mice is indicated (n = 10 mice/group). **(F)** C57BL/6 mice (n = 5) were inoculated with 1×10^6 KPC cells and treated with N6F11 (10 mg/kg; days 10, 14 and 17). A total of 20 mg/kg anti-CD274 antibodies (αCD274) and/or anti-HMGB1 antibodies (αHMGB1) were administered on days 10, 14, and 17. Additionally, 200 μg of anti-CD8 antibodies (αCD8) was administered 1 day before treatment initiation and then twice a week for 3 weeks. Tumor volumes were calculated (n = 5 mice/group; two-way ANOVA with Tukey's multiple comparisons test; data are presented as mean ± SD). **(G)** C57BL/6 mice (n = 5) were inoculated with 1×10^6 MC38 cells and treated with N6F11 (10 mg/kg; days 10, 14 and 17). A total of 20 mg/kg anti-CD274 antibodies (αCD274) and/or anti-HMGB1 antibodies (αHMGB1) were administered on days 10, 14, and 17. Additionally, 200 μg of anti-CD8 antibodies (αCD8) was administered 1 day before treatment initiation and then twice a week for 3 weeks. Tumor volumes were calculated (n = 5 mice/group; two-way ANOVA with Tukey's multiple comparisons test; data are presented as mean ± SD). **(H)** Animal survival was assayed in KPC mice with or without N6F11 (10 mg/kg), IKE (30 mg/kg) and anti-CD274 antibodies (αCD274; 20 mg/kg) treatment (log-rank tests; n = 10 mice/group). Treatment regimens are described in Methods. **(I)** Animal survival was assayed in orthotopic KPC model with or without N6F11 (10 mg/kg) and anti-CD274 antibodies (αCD274; 20 mg/kg) treatment (log-rank tests; n = 10 mice/group). Treatment regimens are described in Methods.

Table S1. Reagent sources

REAGENT or RESOURCE	SOURCE	IDENTIFIER
Chemicals		
Erastin	Selleck Chemicals	S7242
Fin56	Selleck Chemicals	S8254
Ferrostatin-1	Selleck Chemicals	S7243
Liproxstatin-1	Selleck Chemicals	S7699
Tocopherol	Selleck Chemicals	S6104
Deferoxamine	Selleck Chemicals	S5742
Chloroquine	Selleck Chemicals	S6999
Z-VAD-FMK	Selleck Chemicals	S7023
MG132	Selleck Chemicals	S2619
Carfilzomib	Selleck Chemicals	S2853
Bortezomib	Selleck Chemicals	S1013
Necrosulfonamide	Selleck Chemicals	S8251
Staurosporine	Selleck Chemicals	S1421
RSL3	MedChemExpress	HY-100218A
TOFA	MedChemExpress	HY-101068
IKE	Selleck Chemicals	S8877
Cycloheximide	Selleck Chemicals	S7418
CCT137690	Selleck Chemicals	S2744
BODIPY 581/591 C11	Thermo Fisher Scientific	D3861
Click-It LAA	Thermo Fisher Scientific	C10446
Hoechst 33342	Thermo Fisher Scientific	62249
Propidium iodide	Thermo Fisher Scientific	R37108
PBS	Sigma-Aldrich	P5493
DMEM	Thermo Fisher Scientific	11995073
RPMI 1640	Thermo Fisher Scientific	11875119
DMSO	Sigma-Aldrich	472301
Cell lysis buffer	Cell Signaling Technology	9803
Radioimmunoprecipitation assay buffer	Cell Signaling Technology	9806
Protease and phosphatase inhibitor single-use cocktail	Thermo Fisher Scientific	78442
XT MES running buffer	Bio-Rad	1610789
PVDF membranes	Bio-Rad	1620233
SuperSignal West Femto Maximum Sensitivity Substrate	Thermo Fisher Scientific	34095
SuperSignal West Pico Chemiluminescent Substrate	Thermo Fisher Scientific	34080
ssoFast EvaGreen Supermix	Bio-Rad	172-5204
Lipofectamine 3000	Thermo Fisher Scientific	L3000-015

Crystal violet	Sigma-Aldrich	C0775
Recombinant human His6-ubiquitin E1 enzyme (UBE1)	R&D Systems	E-304-050
Recombinant human UbcH5b/UBE2D2 – ubiquitin charged protein	R&D Systems	E2-801-100
Recombinant human His6-Ubc13/UBE2N-Uev1a complex	R&D Systems	E2-664
Recombinant human ubiquitin protein	R&D Systems	U-100H
Recombinant human GPX4 protein	Cayman	26906
Tris(2-carboxyethyl)phosphine hydrochloride	Sigma-Aldrich	C4706-2G
HisPur Ni-NTA resin	Thermo Fisher Scientific	88221
Antibodies		
GPX4	Abcam	ab125066
GPX4	Abcam	ab16739
SLC7A11	Abcam	Ab37185
MAP1LC3A/B	Cell Signaling Technology	4108
ATG5	Cell Signaling Technology	12994
ATG7	Cell Signaling Technology	8558
CLYD	Cell Signaling Technology	8462
p-CYLD	Cell Signaling Technology	4500
MLKL	Cell Signaling Technology	14993
p-MLKL	Cell Signaling Technology	91689
p-EIF2AK3	Cell Signaling Technology	3179
p-EIF2A	Cell Signaling Technology	3398
GFP	Cell Signaling Technology	2555
TP53	Cell Signaling Technology	9282
DDIT3	Cell Signaling Technology	2895
Deubiquitinase antibody sample kit	Cell Signaling Technology	8353
Cleaved PARP	Cell Signaling Technology	5625
Cleaved caspase 3	Cell Signaling Technology	9664
NFE2L2	Cell Signaling Technology	12721
HA-Tag	Cell Signaling Technology	2367
HA-Tag	Cell Signaling Technology	3724
Flag-Tag	Cell Signaling Technology	8146
Flag-Tag	Cell Signaling Technology	14793
ACTB	Cell Signaling Technology	3700
TRIM25	Abclonal	12938
AIMF2	Sigma-Aldrich	SAB4503389
POR	Sigma-Aldrich	SAB1410996
RIPK3	Sigma-Aldrich	AV31513
CD8	BioXcell	BE0061
CD8	Cell Signaling Technology	98941
CD4	BioXcell	BE0003-1

Ly6G	BioXcell	BE0075-1
HMGB1	Kevin Tracey	N/A
CD274	BioLegend	124318
Anti-mouse IgG secondary antibodies, HRP-linked	Cell Signaling Technology	7076
Anti-rabbit IgG secondary antibodies, HRP-linked	Cell Signaling Technology	7074
Anti-rabbit IgG (H+L), DyLight 680 conjugate	Cell Signaling Technology	5366
Anti-mouse IgG (H+L), DyLight 800 conjugate	Cell Signaling Technology	5257
Critical Commercial Assays		
HMGB1 ELISA Kit	Shino-Test Corporation	ST51011
GPX4 ELISA Kit	LSBio	LS-F53129-1
IFNG ELISA Kit	R&D Systems	MIF00
IL2 ELISA Kit	R&D Systems	M2000
Selenium ELISA Kit	Abbexa	abx298910
GSH Assay Kit	Abcam	ab239727
GPX Assay Kit	Abcam	ab102530
iScript Cdna Synthesis Kit	Bio-Rad	1708890
MDA Assay Kit	Sigma-Aldrich	MAK085
BCA Assay Kit	Thermo Fisher Scientific	23225
Cell Counting Kit-8	Bimake	B34304
Q5 Site-Directed Mutagenesis Kit	New England Biolabs	E0554S
Matrigel	Sigma Aldrich	CLS354277
4%-12% Criterion XT Bis-Tris gels	Bio-Rad	3450124
E.Z.N.A. HP Total RNA Kit	Omega Bio-Tek	R6812
Experimental Models: Cell Lines and Primary Immune Cells		
HT1080	ATCC	CCL-121
PANC1	ATCC	CRL-1469
MiaPACA2	ATCC	CRL-1420
BxPC3	ATCC	CRL-1687
5637	ATCC	HTB-9
Hs578T	ATCC	HTB-126
HeLa	ATCC	CCL-2
MC38	Lin Zhang	N/A
Atg5$^{-/-}$ MEFs	Noboru Mizushima	N/A
Atg7$^{-/-}$ MEFs	Noboru Mizushima	N/A
Ripk3$^{-/-}$ MEFs	Douglas R. Green	N/A
Gpx4$^{-/-}$ Pfa-1 cells	Marcus Conrad	N/A
KPC	David Tuveson	N/A
293FT	Thermo Fisher Scientific	R70007
DC2.4 cells	MilliporeSigma	SCC142
Human peripheral blood DCs	STEMCELL Technologies	70041

Human peripheral $CD8^+$ T cells	STEMCELL Technologies	200-383
Human peripheral NK cells	STEMCELL Technologies	200-0063
Experimental Models: Organisms		
C57BL/6J WT mice	The Jackson Laboratory	000664
C57BL/6J *Rag1*$^{-/-}$ mice	The Jackson Laboratory	034159
Kras$^{G12D/+}$ mice (B6.129S4-Kras^{tm4Tyj}/J)	The Jackson Laboratory	008179
Pdx1-Cre mice (B6.FVB-Tg(Pdx1-cre)^{6Tuv}/J)	The Jackson Laboratory	014647
KPC mice	David Tuveson	N/A
Software and Algorithms		
Image Lab software version 6.1	Bio-Rad	N/A
Prism version 8.4.3	GraphPad	N/A
CFX Manager software 2.0	Bio-Rad	N/A
Image J 1.52v	NIH	N/A
Mascot search engine 2.4.0	Matrix Science Ltd.	N/A
Empiria Studio Software 2.2	LI-COR	N/A

Table S2. Oligonucleotides, primers and cDNA

REAGENT or RESOURCE	SOURCE	IDENTIFIER
Oligonucleotides		
TRIM25-shRNA1 (sequence: CGGGAACTGAACCACAAGCTGATACTCGAGTATCAGCTTGTGGTTCAGTTCTTTTTG)	Sigma-Aldrich	This paper
TRIM25-shRNA2 (sequence: CCGGGAGTGAGATCCAGACCTTGAACTCGAGTTCAAGGTCTGGATCTCACTCTTTTTG)	Sigma-Aldrich	This paper
CYLD-shRNA1 (sequence: CCGGTCTATTGCACATCAATGTATCTCGAGATATCATTGATGTGCAATAGATTTTTG)	Sigma-Aldrich	This paper
CYLD-shRNA2 (sequence: CCGGTACTTAGACTCAACCTTATTCCTCGAGGAATAAGGTTGAGTCTAAGTATTTTTG)	Sigma-Aldrich	This paper
EIF3I shRNA (sequence: CCGGGTGAGCTGAGATCACGTCATTCTCGAGAATGACGTGATCTCAGCTCACTTTTTG)	Sigma-Aldrich	This paper
TRIM25-sgRNA1 (sequence: AGGCGGGGCTGTCGAAGTG)	Sigma-Aldrich	This paper
TRIM25-sgRNA2 (sequence: CGGCGCAACAGGTCGCGAA)	Sigma-Aldrich	This paper
Primers		
GPX4 primers: 5'-TTCCCGTGTAACCAGTTCGG-3' and GTGGAGAGACGGTGTCCAAA-3'	Sigma-Aldrich	This paper
RNA18S (sequence: 5'-CTACCACATCCAAGGAAGCA-3' and 5'-TTTTTCGTCACTACCTCCCCG-3')	Sigma-Aldrich	This paper
EIF3I (sequence: 5'-CAGAACGTCCTGTCAACTCAGC-3' and 5'-CTTGCCAATCCTGGTGGAGGTT-3')	Sigma-Aldrich	This paper
CD80 (sequence: 5'-CCTCAAGTTTCCATGTCCAAGGC-3' and 5'-GAGGAGAGTTGTAACGGCAAGG-3')	Sigma-Aldrich	This paper
CD86 (sequence: 5'-ACGTATTGGAAGGAGATTACAGCT-3' and 5'-TCTGTCAGCGTTACTATCCCGC-3')	Sigma-Aldrich	This paper
TRIM25-RING primers: 5'-TAGGCAGGCTGTAGGCAC-3' and 5'-CACATCATCCAGTGCTCTCG-3'	Sigma-Aldrich	This paper
TRIM25-CC primers: 5'-ATGACAAGCATATGCTCCGC	Sigma-Aldrich	This paper

GCCGTCTACCAGGC-3' and 5'-TATCTAGATGTACAGCTAGGC CTTGAGAGATGTTGAG-3'		
TRIM25-PS primers: 5'-TTTCTGGAGAAAGCATCAAAAC-3' and 5'-GAGCTTGTCGTCATCGTC-3'	Sigma-Aldrich	This paper
TRIM25-△PS primers: 5'-TAGGCAGGCTGTAGGCAC-3' and 5'-CTCGAACTCATCCCTCTTGG-3'	Sigma-Aldrich	This paper
TRIM25-shRO primers: 5'-taaactcatcAAAGGCATCCACCAGAGC-3' and 5'-tgattgagctcCACCTCGGGGATGTAGAC-3'	Sigma-Aldrich	This paper
TRIM25-CS5053 mutant primers: 5'-cagtccCGCGCCGTCTACCAGGCG-3' and 5'-cggggaCAGGTATGGCGAGCCCTGG-3'	Sigma-Aldrich	This paper
GPX4-K48 mutant primers: 5'-CCAGTGAGGCaggACCGAAGTAAAC-3' and 5'-GAGGCCACGTTGGTGACG-3'	Sigma-Aldrich	This paper
GPX4-K125 mutant primers: 5'-GATCCAACCCaggGGCAAGGGCA-3' and 5'-TTCATCCACTTCCACAGCGGG-3'	Sigma-Aldrich	This paper
GPX4-K127 mutant primers: 5'-ACCCAAGGGCaggGGCATCCTGG-3' and 5'-TGGATCTTCATCCACTTCCACAGCG-3'	Sigma-Aldrich	This paper
GPX4-K135 mutant primers: 5'-AAATGCCATCaggTGGAACTTCACCAAG-3' and 5'-CCCAGGATGCCCTTGCCC-3'	Sigma-Aldrich	This paper
GPX4-K127 mutant primers: 5'-CTGCGTGGTGaggCGCTACGGAC-3' and 5'-CCGTTCTTGTCGATGAGGAACTTGG-3'	Sigma-Aldrich	This paper
cDNA		
GFP-GPX4 cDNA	Brent R. Stockwell	N/A
FLAG-TRIM25 (pFlagCMV2-EFP)	Dong-Er Zhang	Addgene:12449
Prk5-HA-ubiquitin-WT	Addgene	17608
pRK5-HA-ubiquitin-K48	Addgene	17605
pRK5-HA-ubiquitin-K63	Addgene	17606
LentiCas9-Blast	Addgene	52962
RIPK3 cDNA	Addgene	78804